JOURNAL OF COMPUTATIONAL PHYSICS **145,** 693–730 (1998)
ARTICLE NO. CP986051

A Dynamic LES Scheme for the Vorticity Transport Equation: Formulation and *a Priori* Tests

John R. Mansfield,[1] Omar M. Knio,[2] and Charles Meneveau

Department of Mechanical Engineering, Johns Hopkins University, Baltimore, Maryland 21218-2686
E-mail: knio@jhu.edu

Received November 18, 1997; revised May 21, 1998

This work aims at the development of a Lagrangian large eddy simulation (LES) scheme. The scheme is based on the filtered vorticity transport equation and on modeling the effects of subfilter scale (SFS) velocity and vorticity fluctuations using a dynamic eddy diffusivity model. The dynamic implementation of the model relies on multiple filtering in order to determine model coefficients from the resolved data. The performance of the dynamic SFS model is examined using *a priori* tests that are based on direct numerical simulations of forced, homogeneous, isotropic turbulence. The tests show a fair correlation of the model with SFS convection of vorticity. In addition, the computed value of the dynamic model coefficient is in good agreement with predictions based on enstrophy balances. Finally, the direct numerical simulation data is used to compare a three-dimensional particle representation of the model with spectral evaluations. The tests show that when the particle representation is sufficiently resolved, the Lagrangian model predictions are in good agreement with spectral results.

1. INTRODUCTION

Large eddy simulation (LES) generally aims at overcoming the scale disparity of turbulent flow by numerically solving equations which describe the evolution of the large scales of motion. A widespread LES approach is based on spatially filtering the equations of motion [1–3]. Due to the convective nonlinearity of the momentum equations, a stress term appears in the filtered equations which includes direct contributions from unresolved scales. This unknown stress must be modeled exclusively in terms of resolved, large-scale quantities; this is the analogue of the well-known closure problem which affects the Reynolds-averaged

[1] Present address: Mechanical and Aerospace Engineering, UCLA, Los Angeles, CA 90095-1597.
[2] Corresponding author.

0021-9991/98 $25.00

equations of motion. When filtering and spatial differentiation commute, the governing equations for LES take the form of the original equations, together with a model term. The effectiveness of LES depends, in particular, on the effectiveness of the model in representing the impact of unresolved scales.

Most previous applications of LES have been performed using grid-based approximations of the filtered Navier–Stokes equations. On the other hand, despite recent interest in Eulerian vorticity-based formulations (e.g. [4–6]) LES of the vorticity transport equation remains scarce. However, particle-based, Lagrangian large eddy simulations have been attempted. The original efforts towards the development of numerical methods for Lagrangian LES are due to Chorin [7, 8]. These have led, in particular, to the well-known "hairpin-removal" schemes. The latter are motivated by renormalization of the vorticity evolution equations which, like spatial filtering, aims at "absorbing" the effect of the smallest lengthscales by constructing "effective" equations of motion. In its basic form, Chorin's hairpin removal scheme essentially consists of a filament-based simulation, together with a local mesh redistribution algorithm. The redistribution algorithm acts on the geometry of the filaments by removing the smallest scales, which are typically in the form of hairpin vortices. Recently proposed extensions [9] of the hairpin removal algorithm include the incorporation of renormalized Biot–Savart interaction which accounts for the removal (renormalization) process.

Hairpin removal schemes have been applied in a variety of conditions, including both bounded [10] and free shear flows [11]. A similar approach has been recently proposed by Fernandez *et al.* [12], based on the combination of a vortex filament scheme with a 3D "filament-surgery" algorithm. The surgery is based on identifying "hairpins" (or locally collapsed regions) with local minima of the energy density along the filament, and locally removing them by remeshing the filament.

In this paper, an alternative approach to Lagrangian LES is explored. We follow a similar approach to the grid-based LES in primitive variables and start with the filtered vorticity transport equation. As discussed in Section 2, the filtering operation leads to the definition of a subfilter scale (SFS) torque which accounts for unresolved velocity and vorticity fluctuations. A dynamic eddy-diffusivity model is then proposed in order to represent the SFS torque which is due to these fluctuations. In fact, Winckelmans *et al.* [13] have recently compared nondynamic eddy–viscosity models for the velocity–pressure and the velocity–vorticity formulations of LES and concluded that the latter were potentially more realistic. The primary objective in the present paper is to examine the suitability of a Lagrangian formulation of a dynamic eddy diffusivity model. As outlined in Section 3, the Lagrangian formulation is based on a particle representation of the vorticity field. In Section 4 the dynamic eddy diffusivity model is first analyzed using *a priori* tests, based on results of direct numerical simulation (DNS) of forced isotropic turbulence. In Section 5 the DNS data is used to examine a particle representation of the SFS model and of the dynamic model coefficient. We restrict our attention to *a priori* tests of the Lagrangian model; implementation of the particle scheme will be discussed elsewhere [14]. Major conclusions are summarized in Section 6.

2. FORMULATION

2.1. *LES of Momentum Equations*

In order to clearly outline the present construction, we start with a brief description of LES of the momentum equations in primitive variables. As mentioned in the Introduction, this

approach is typically based on solutions of the filtered Navier–Stokes equations [1, 2, 15],

$$\nabla \cdot \tilde{\boldsymbol{u}} = 0, \tag{1}$$

$$\frac{\partial \tilde{\boldsymbol{u}}}{\partial t} + \tilde{\boldsymbol{u}} \cdot \nabla \tilde{\boldsymbol{u}} = -\frac{1}{\rho}\nabla \tilde{p} + \nu \nabla^2 \tilde{\boldsymbol{u}} + \tilde{\boldsymbol{\mathcal{F}}} - \nabla \cdot \boldsymbol{\tau}, \tag{2}$$

where $\boldsymbol{u}$ is the velocity vector, t is time, ρ is density, p is pressure, ν is the kinematic viscosity, $\boldsymbol{\mathcal{F}}$ is a body force term, and

$$\tau_{ij} = \widetilde{u_i u_j} - \tilde{u}_i \tilde{u}_j \tag{3}$$

is the subgrid scale (SGS), or subfilter scale stress. Here and in the following, tildes are used to denote spatially filtered quantities. Following [1, 2, 15] filtering is assumed to be based on a convolution of the form

$$\tilde{q}(\boldsymbol{x}, t) = \int G_\Delta(|\boldsymbol{x} - \boldsymbol{x}'|) q(\boldsymbol{x}', t)\, d^3\boldsymbol{x}', \tag{4}$$

where q is the quantity being filtered. We also assume that the "grid filter" G_Δ is a homogeneous, smooth, and rapidly decaying radial function and that the force field $\boldsymbol{\mathcal{F}}$ acts at large scales only, i.e. $\tilde{\boldsymbol{\mathcal{F}}} \equiv \boldsymbol{\mathcal{F}}$.

In order to close the equation system (1)–(2), one needs to provide a model of the unknown SGS stress $\boldsymbol{\tau}$, or its divergence $\nabla \cdot \boldsymbol{\tau}$, in terms of the filtered velocity field $\tilde{\boldsymbol{u}}$. A well-known model for the deviatoric part of the SGS stress is the Smagorinsky eddy viscosity model [16],

$$\tau_{ij} - (\delta_{ij}/3)\tau_{kk} = -2\nu_\mathsf{T}\tilde{\mathsf{S}}_{ij}, \tag{5}$$

$$\nu_\mathsf{T} = C_s^2 \Delta^2 |\tilde{\mathbf{S}}|, \tag{6}$$

where $|\mathbf{S}| \equiv \sqrt{2\mathsf{S}_{mn}\mathsf{S}_{mn}}$ denotes the modulus of the strain-rate tensor. Typically, the constant C_s is prescribed; "standard" values are around 0.15 [2, 15].

An alternative to prescribing the model constant C_s is based on the so-called dynamic procedure [17], which relies on multiple filtering operations to determine C_s from the simulated fields. Thus, an additional filtering operation, called the test filter, is introduced. The test filter, which has width $\Delta' > \Delta$, is denoted by an overbar and is given by

$$\bar{\boldsymbol{u}}(\boldsymbol{x}, t) = \int G_{\Delta'}(|\boldsymbol{x} - \boldsymbol{x}'|) \boldsymbol{u}(\boldsymbol{x}', t)\, d^3\boldsymbol{x}'. \tag{7}$$

Applying the combined grid and test filters to the Navier–Stokes equations introduces a stress at scale Δ',

$$\mathsf{T}_{ij} = \overline{\widetilde{u_i u_j}} - \bar{\tilde{u}}_i \bar{\tilde{u}}_j. \tag{8}$$

The SGS stresses at the two filter levels Δ and Δ' are linked by the Germano identity [17],

$$\mathsf{L}_{ij} = \mathsf{T}_{ij} - \bar{\boldsymbol{\tau}}_{ij} = \overline{\tilde{u}_i \tilde{u}_j} - \bar{\tilde{u}}_i \bar{\tilde{u}}_j. \tag{9}$$

Note that Eq. (9) involves $\tilde{\boldsymbol{u}}$ only, so that evaluation of $\mathbf{L}$ does not require knowledge of the unfiltered velocity $\boldsymbol{u}$. Assuming that $\mathbf{T}$ can be modeled in a similar fashion as $\boldsymbol{\tau}$, and that C_s is locally independent of the width of the test filter, one obtains

$$C_s^2\left(2\Delta^2\overline{|\tilde{\mathbf{S}}|\tilde{S}_{ij}} - 2\Delta'^2|\bar{\tilde{\mathbf{S}}}|\bar{\tilde{S}}_{ij}\right) = \overline{\tilde{u}_i\tilde{u}_j} - \bar{\tilde{u}}_i\bar{\tilde{u}}_j - \delta_{ij}/3\left(\overline{\tilde{u}_n\tilde{u}_n} - \bar{\tilde{u}}_n\bar{\tilde{u}}_n\right). \tag{10}$$

Since all quantities on the right-hand side of Eq. (10) are resolved, dynamic determination of C_s is possible.

LES using the dynamic Smagorinsky model have been used in various applications (e.g., [18–20]). Of course, other SGS models have been considered for LES; prominent examples include similarity [21, 22] and hyperviscosity [23] models. In particular, similarity and mixed models have been found to reproduce a number of physical features of the SGS stress (e.g., relationships between small scales and coherent structures [24, 25], response to rapid straining [26]). The mixed model has also been shown to perform quite well in simulations of various flows (see, e.g., [27–30]). As a first step, in the present work we will focus only on the dynamic eddy viscosity model and its implementation in a vorticity-based LES scheme. Future extensions include the development of dynamic mixed models in this framework.

2.2. *Vorticity Formulation of LES*

The starting point in the present development of vorticity-based LES is the filtered vorticity transport equation,

$$\frac{\partial\tilde{\omega}_i}{\partial t} + \tilde{u}_j\frac{\partial\tilde{\omega}_i}{\partial x_j} = \tilde{\omega}_j\frac{\partial\tilde{u}_i}{\partial x_j} + \nu\nabla^2\tilde{\omega}_i + [\nabla\times\boldsymbol{\mathcal{F}}]_i - \frac{\partial \mathsf{R}_{ij}}{\partial x_j}, \tag{11}$$

where

$$\mathsf{R}_{ij} \equiv (\widetilde{\omega_i u_j} - \tilde{\omega}_i\tilde{u}_j) - (\widetilde{u_i\omega_j} - \tilde{u}_i\tilde{\omega}_j) \tag{12}$$

is the subgrid scale vorticity stress. The vorticity stress $\mathbf{R}$ accounts for the effect of unresolved velocity *and* vorticity fluctuations. $\mathbf{R}$ is composed of two parts,

$$\mathsf{R}_{ij} = \Phi_{ij} - \Phi_{ji}, \tag{13}$$

where

$$\Phi_{ij} \equiv \widetilde{\omega_i u_j} - \tilde{\omega}_i\tilde{u}_j. \tag{14}$$

Note that Φ_{ji} represents SFS vortex stretching and tilting due to the unresolved motion while Φ_{ij} reflects vortex transport by SFS velocity fluctuations. Also note that Eq. (13) immediately shows that $\mathbf{R}$ is antisymmetric.

2.2.1. Subfilter scale model. As for the filtered momentum equations, one must provide a model for the vorticity stress $\mathbf{R}$ in order to close the filtered vorticity transport equation. Alternatively, one can simply model the divergence of the vorticity stress, $\partial\mathsf{R}_{ij}/\partial x_j$, which

we refer to as the subfilter scale torque. We shall adopt the latter approach and, by analogy with the Smagorinsky model, focus on the following eddy diffusivity model [13, 31],

$$\boldsymbol{g} = -\nabla \times (\nu_{\mathsf{T}} \nabla \times \tilde{\boldsymbol{\omega}}), \tag{15}$$

where

$$\nu_{\mathsf{T}} = C_r^2 \Delta^2 |\tilde{\mathbf{S}}| \tag{16}$$

is the eddy diffusity. Note that by construction the divergence of the SFS torque vanishes identically. Also note that the eddy diffusivity in Eq. (16) is not necessarily identical to the eddy diffusivity in the Smagorinsky model, Eq. (6); the model constants C_r and C_s are used to distinguish between the two quantities. For isotropic turbulence the model coefficient C_r may be analytically estimated, as outlined in Appendix A. The estimated value $C_r = 0.12$ is close to, but somewhat smaller than the standard Smagorinsky constant $C_s \approx 0.15$.

It is also interesting to point out that the SFS torque can be alternatively expressed as

$$g_i = \frac{\partial}{\partial x_j}\left(\nu_{\mathsf{T}} \frac{\partial \tilde{\omega}_i}{\partial x_j}\right) - \frac{\partial \nu_{\mathsf{T}}}{\partial x_j}\frac{\partial \tilde{\omega}_j}{\partial x_i}. \tag{17}$$

Thus, $\boldsymbol{g}$ is expressed as the sum of a gradient-diffusion term and an additional term which corresponds to the scalar product of the gradient of the eddy diffusivity with the transpose of the vorticity gradient. The second term can be thought of as a correction term that is needed to render the SFS torque divergence-free.

2.2.2. Dynamic implementation. As discussed in Section 2.1, implementation of the eddy diffusivity model may either rely on a prescribed model coefficient or on a dynamic evaluation of the model constant. Here, we explore the latter option by adapting the dynamic procedure in [17] to the filtered vorticity transport equation. Briefly, filtering the vorticity transport equation at scale Δ and then at scale Δ' yields

$$\frac{\partial \tilde{\omega}_i}{\partial t} + \tilde{u}_j \frac{\partial \tilde{\omega}_i}{\partial x_j} = \tilde{\omega}_j \frac{\partial \tilde{u}_i}{\partial x_j} + \nu \nabla^2 \tilde{\omega}_i + \epsilon_{ijk} \frac{\partial \mathcal{F}_k}{\partial x_j} + g_i \tag{18}$$

and

$$\frac{\partial \bar{\tilde{\omega}}_i}{\partial t} + \bar{\tilde{u}}_j \frac{\partial \bar{\tilde{\omega}}_i}{\partial x_j} = \bar{\tilde{\omega}}_j \frac{\partial \bar{\tilde{u}}_i}{\partial x_j} + \nu \nabla^2 \bar{\tilde{\omega}}_i + \epsilon_{ijk} \frac{\partial \mathcal{F}_k}{\partial x_j} + G_i, \tag{19}$$

respectively, where $\boldsymbol{G}$ is the SFS torque at scale Δ'. We now assume that the SFS torques $\boldsymbol{g}$ and $\boldsymbol{G}$ can be modeled as in Eq. (15) with the same model coefficient; we thus have

$$g_i = C_r^2 \Delta^2 \left[\frac{\partial}{\partial x_j}\left(\sqrt{2\tilde{\mathsf{S}}_{mn}\tilde{\mathsf{S}}_{mn}}\frac{\partial \tilde{\omega}_i}{\partial x_j}\right) - \frac{\partial}{\partial x_j}\left(\sqrt{2\tilde{\mathsf{S}}_{mn}\tilde{\mathsf{S}}_{mn}}\right)\frac{\partial \tilde{\omega}_j}{\partial x_i}\right] \tag{20}$$

and

$$G_i = C_r^2 \Delta'^2 \left[\frac{\partial}{\partial x_j}\left(\sqrt{2\bar{\tilde{\mathsf{S}}}_{mn}\bar{\tilde{\mathsf{S}}}_{mn}}\frac{\partial \bar{\tilde{\omega}}_i}{\partial x_j}\right) - \frac{\partial}{\partial x_j}\left(\sqrt{2\bar{\tilde{\mathsf{S}}}_{mn}\bar{\tilde{\mathsf{S}}}_{mn}}\right)\frac{\partial \bar{\tilde{\omega}}_j}{\partial x_i}\right]. \tag{21}$$

Next, Eq. (18) is filtered as scale Δ' and the result is subtracted from Eq. (19), leading to

$$(\overline{\tilde{\boldsymbol{u}} \cdot \nabla \tilde{\boldsymbol{\omega}}} - \bar{\tilde{\boldsymbol{u}}} \cdot \nabla \bar{\tilde{\boldsymbol{\omega}}}) - (\overline{\tilde{\boldsymbol{\omega}} \cdot \nabla \tilde{\boldsymbol{u}}} - \bar{\tilde{\boldsymbol{\omega}}} \cdot \nabla \bar{\tilde{\boldsymbol{u}}}) = \bar{\boldsymbol{g}} - \boldsymbol{G}. \tag{22}$$

Substituting the model definitions in Eqs. (20) and (21), and factoring the model coefficient, C_r, we get

$$\boldsymbol{l} = C_r^2 \boldsymbol{m}, \tag{23}$$

where

$$\boldsymbol{l} = \boldsymbol{l}^{\mathsf{C}} + \boldsymbol{l}^{\mathsf{S}} \tag{24}$$

$$\boldsymbol{l}^{\mathsf{C}} \equiv (\overline{\tilde{\boldsymbol{u}} \cdot \nabla \tilde{\boldsymbol{\omega}}} - \bar{\tilde{\boldsymbol{u}}} \cdot \nabla \bar{\tilde{\boldsymbol{\omega}}}), \tag{25}$$

$$\boldsymbol{l}^{\mathsf{S}} \equiv -(\overline{\tilde{\boldsymbol{\omega}} \cdot \nabla \tilde{\boldsymbol{u}}} - \bar{\tilde{\boldsymbol{\omega}}} \cdot \nabla \bar{\tilde{\boldsymbol{u}}}), \tag{26}$$

$$\boldsymbol{m} = \boldsymbol{m}^{\mathsf{D}} + \boldsymbol{m}^{\mathsf{Z}}, \tag{27}$$

$$\boldsymbol{m}^{\mathsf{D}} \equiv \Delta^2 \overline{\nabla \cdot (|\tilde{\mathbf{S}}| \nabla \tilde{\boldsymbol{\omega}})} - \Delta'^2 \nabla \cdot (|\bar{\tilde{\mathbf{S}}}| \nabla \bar{\tilde{\boldsymbol{\omega}}}), \tag{28}$$

and

$$\boldsymbol{m}^{\mathsf{Z}} \equiv -(\Delta^2 \overline{(\nabla |\tilde{\mathbf{S}}|) \cdot (\nabla \tilde{\boldsymbol{\omega}})^{\mathsf{T}}} - \Delta'^2 (\nabla |\bar{\tilde{\mathbf{S}}}|) \cdot (\nabla \bar{\tilde{\boldsymbol{\omega}}})^{\mathsf{T}}). \tag{29}$$

Note that $\boldsymbol{l}$ and $\boldsymbol{m}$ involve resolved quantities only and that the only "unknown" in Eq. (23) is C_r. However, Eq. (23) is a vector equality; i.e., C_r is overspecified. This difficulty is tackled by selecting C_r so as to minimize the average square error [32, 33], $\langle \boldsymbol{e} \cdot \boldsymbol{e} \rangle$, where

$$\boldsymbol{e} \equiv \boldsymbol{l} - C_r^2 \boldsymbol{m}. \tag{30}$$

Differentiating the mean-square error with respect to C_r^2 and assuming that the model constant can be factored out of the filtering and averaging operators (for a discussion of the limitations of this assumption, see [33]), we get

$$\begin{aligned} \frac{\partial}{\partial C_r^2} \langle \boldsymbol{e} \cdot \boldsymbol{e} \rangle &= \frac{\partial}{\partial C_r^2} \langle \boldsymbol{l} \cdot \boldsymbol{l} \rangle - 2 \frac{\partial}{\partial C_r^2} \left(C_r^2 \langle \boldsymbol{l} \cdot \boldsymbol{m} \rangle \right) + \frac{\partial}{\partial C_r^2} \left(C_r^4 \langle \boldsymbol{m} \cdot \boldsymbol{m} \rangle \right) \\ &= -2 \langle \boldsymbol{l} \cdot \boldsymbol{m} \rangle + 2 C_r^2 \langle \boldsymbol{m} \cdot \boldsymbol{m} \rangle. \end{aligned}$$

Thus, the mean square error is minimized when

$$C_r^2 = \langle \boldsymbol{l} \cdot \boldsymbol{m} \rangle / \langle \boldsymbol{m} \cdot \boldsymbol{m} \rangle. \tag{31}$$

This completes the formulation of the dynamic model.

Note that there may be several choices for the averaging operation, including spatial averaging [17, 33] and averaging over particle trajectories [34]. For simplicity we restrict our attention to simple spatial averaging, although Lagrangian averaging appears as a natural candidate for future studies.

3. PARTICLE DISCRETIZATION

As mentioned in the Introduction, one of the motivations of the present work is the implementation of the SFS vorticity model in a Lagrangian vortex method. In this section we focus on formulating an appropriate particle discretization of the SFS model, whose performance will be later tested against the predictions of finite-difference and spectral approximations. The approach adopted below closely follows well-known vortex element constructions; see reviews in [35–37]. Thus, we start with a brief summary of the Lagrangian discretization and then discuss the model implementation.

3.1. *Vortex Method*

The three-dimensional vortex element method is a Lagrangian technique for the simulation of the vorticity transport equation:

$$\frac{\partial \boldsymbol{\omega}}{\partial t} + \boldsymbol{u} \cdot \nabla \boldsymbol{\omega} = \boldsymbol{\omega} \cdot \nabla \boldsymbol{u} + \nu \nabla^2 \boldsymbol{\omega}. \tag{32}$$

In its simplest form, the method is used in an unbounded space with no internal boundaries, where the velocity is given by the Biot–Savart law [38]:

$$\boldsymbol{u}(\boldsymbol{x}) = -\frac{1}{4\pi} \int \frac{(\boldsymbol{x} - \boldsymbol{x}') \times \boldsymbol{\omega}(\boldsymbol{x}')}{|\boldsymbol{x} - \boldsymbol{x}'|^3}\, d^3\boldsymbol{x}'. \tag{33}$$

The essential feature of the vortex method used in the present work is the representation of the vorticity field using a finite number, N, of desingularized vortex elements. The vortex elements are specified in terms of their position vector $\boldsymbol{X}_i$, strength $\boldsymbol{\zeta}_i$, and volume dV_i. The elements induce a smooth approximation to the vorticity field, according to [39, 40],

$$\boldsymbol{\omega}^{\mathrm{N}}(\boldsymbol{x}, t) = \sum_{i=1}^{N} \boldsymbol{\zeta}_i(t)\, dV_i\, f_\delta(\boldsymbol{x} - \boldsymbol{X}_i(t)), \tag{34}$$

where

$$f_\delta(\boldsymbol{x}) \equiv \frac{1}{\delta^3} f\left(\frac{|\boldsymbol{x}|}{\delta}\right) \tag{35}$$

is a spherical rapidly decaying core function and δ is the core radius. The function f is also assumed to satisfy some moment conditions [40, 41] which govern the convergence of the scheme.

The vorticity distribution in Eq. (34) induces a smooth velocity field given by the desingularized Biot–Savart law,

$$\boldsymbol{u}(\boldsymbol{x}) = -\frac{1}{4\pi} \sum_{i=1}^{N} \frac{(\boldsymbol{x} - \boldsymbol{X}_i) \times \boldsymbol{\zeta}_i}{|\boldsymbol{x} - \boldsymbol{X}_i|^3}\, dV_i \kappa_\delta(\boldsymbol{x} - \boldsymbol{X}_i), \tag{36}$$

where

$$\kappa_\delta(\boldsymbol{x}) \equiv \kappa\left(\frac{|\boldsymbol{x}|}{\delta}\right), \quad \kappa(r) = 4\pi \int_0^r \xi^2 f(\xi)\, d\xi \tag{37}$$

is the velocity smoothing kernel corresponding to f [40]. In all of the computations below,

we shall rely on the third-order Gaussian core function [42],

$$f(r) = \frac{3}{4\pi} \exp(-r^3) \tag{38}$$

with corresponding velocity kernel

$$\kappa(r) = 1 - \exp(-r^3). \tag{39}$$

As shown by Beale and Majda [40], this choice of f and κ leads to an "essentially second-order" particle discretization.

Using the particle representation of the velocity and vorticity field, the 3D vortex method then transforms the original system (32)–(33) into a system of evolution equations for the particle positions and strengths. The evolution of the flow is determined by integrating

$$\frac{d\boldsymbol{X}_i}{dt} = \boldsymbol{u}(\boldsymbol{X}_i) \tag{40}$$

$$\frac{d\boldsymbol{\zeta}_i}{dt} = \boldsymbol{\zeta}_i \cdot \nabla \boldsymbol{u}(\boldsymbol{X}_i) + \nu D[\boldsymbol{\zeta}_i]; \tag{41}$$

i.e. by moving the elements along particle trajectories and modifying their strengths according to the vorticity transport equation. Here, $D[\boldsymbol{\zeta}_i]$ is the Lagrangian representation of the Laplacian [43].

Below, we will explore how the particle representation of the vorticity field can be understood as a spatial filtering operation and, hence, exploited to dynamically determine the coefficient of the SFS model. To this end, it is first necessary to specify the meaning of various filtering operations in the present Lagrangian context.

3.2. *Grid and Test Filtering*

In Eulerian grid-based schemes, resolution is limited to the mesh spacing, quantities represented on the computational grid are commonly considered to be "grid-filtered," and the filter width Δ is identified with the mesh size. In most situations, the precise relationship between the filtering operation and the numerical discretization is either not established, or stated in an *ad hoc* fashion. A similar issue arises for Lagrangian particle discretizations. However, the situation differs due to the introduction of smoothing functions with a core size that is larger than the particle spacing. Here, it is natural to associate the resolution limit with the core radius, δ, and to consider the Lagrangian representation of the vorticity field $\boldsymbol{\omega}^{\mathrm{N}}$ in Eq. (34) to be "particle filtered." The correspondence between the filtering and the numerical representation can be further clarified by noting that the Lagrangian representation in Eq. (34) is a discretized version of the approximate identity:

$$\boldsymbol{\omega}(\boldsymbol{x}) \equiv \delta(\boldsymbol{x}) * \boldsymbol{\omega}(\boldsymbol{x}) = \lim_{\delta \to 0} f_\delta(\boldsymbol{x}) * \boldsymbol{\omega}(\boldsymbol{x}) = \lim_{\delta \to 0} \tilde{\boldsymbol{\omega}}(\boldsymbol{x}) \tag{42}$$

where $*$ denotes the convolution operator. Thus, at finite δ it is appropriate to interpret $\boldsymbol{\omega}^{\mathrm{N}}(\boldsymbol{x}) \approx \tilde{\boldsymbol{\omega}}(\boldsymbol{x})$ as the filtered vorticity, and the core smoothing function as the spatial filter.

The convection velocity in Eq. (40) is taken as the filtered velocity field. In this fashion, the total derivative in Eq. (41) includes the convective derivative with a convection velocity equal to the filtered velocity field, as in the left-hand side of Eq. (11). The effects of subfilter

scale velocity and vorticity fluctuations on the transport of filtered vorticity are accounted for in Φ_{ij}. Alternatively, one could seek formulations in which the SFS model is written in terms of a diffusion velocity. Thus, the effects of unresolved motion would be accounted for in the equation describing the motion of the elements while the SFS term would drop out of the evolution equation for the vortex strengths. We shall not explore such approaches in the present work.

In order to compare different filters it is useful to "standardize" the definition of the filter size. Specifically, we seek to relate the vortex element core size to the width Δ of an "equivalent" box filter. We introduce a scaling coefficient c, such that $\Delta = c\delta$, and define a particle filter G_Δ using

$$G_\Delta(\boldsymbol{x}) \equiv f_{\Delta/c}(\boldsymbol{x}) = \frac{3}{4\pi}\left(\frac{c}{\Delta}\right)^3 \exp\left[-\left(\frac{c|\boldsymbol{x}|}{\Delta}\right)^3\right]. \tag{43}$$

The constant c is determined by requiring that the particle filter G_Δ has the same characteristic size as the spherical box filter,

$$B_\Delta(\boldsymbol{x}) = \begin{cases} \frac{6}{\pi\Delta^3}, & \text{if } |\boldsymbol{x}| \le \Delta/2, \\ 0, & \text{otherwise.} \end{cases} \tag{44}$$

This requirement is satisfied when the energy contents of the transforms $\hat{G}_\Delta$ and $\hat{B}_\Delta$ are the same, i.e. when

$$\int |\hat{G}_\Delta(\boldsymbol{k})|^2 \, d^3\boldsymbol{k} = \int |\hat{B}_\Delta(\boldsymbol{k})|^2 \, d^3\boldsymbol{k}. \tag{45}$$

For the third-order Gaussian in Eq. (43), numerical evaluation of the above integrals yields $c = 2.88243$. Thus, the relationship between the core size and the (standardized) filter size is $\Delta = 2.88\delta$. Figure 1 compares the particle and the spherical box filters.

In the implementation of the dynamic model, application of a test filter is necessary. Here, the test filter is assumed to have the same shape as the particle filter. The action of the test filter is defined by

$$\bar{q}(\boldsymbol{x}) = \frac{\sum_{i=1}^{N} q(\boldsymbol{X}_i) \exp\left[-(c|\boldsymbol{x} - \boldsymbol{X}_i|/\Delta')^3\right]}{\sum_{i=1}^{N} \exp\left[-(c|\boldsymbol{x} - \boldsymbol{X}_i|/\Delta')^3\right]}, \tag{46}$$

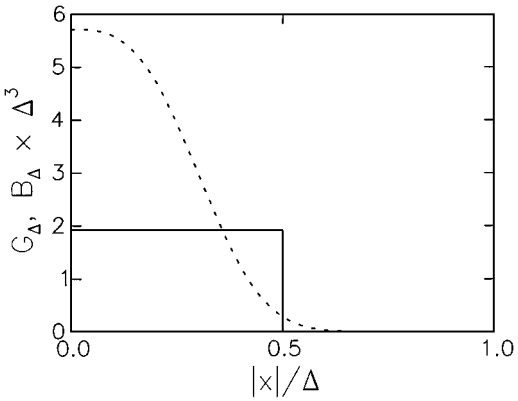

FIG. 1. Comparison of the spherical box filter, B, and the particle filter, G. The spherical box filter is shown using a solid line, while the particle filter is shown using a dashed line.

where q is the quantity being test-filtered and Δ' is the width of the test filter. Note that both the particle filter and test filter are defined in terms of the particle positions and strengths.

3.3. *Evaluation of C_r*

In order to determine the model constant C_r dynamically one must evaluate, based on the Lagrangian particle data, the quantities $\boldsymbol{l}^{\mathsf{C}}$, $\boldsymbol{l}^{\mathsf{S}}$, $\boldsymbol{m}^{\mathsf{D}}$, and $\boldsymbol{m}^{\mathsf{Z}}$, defined in Eqs. (25), (26), (28), and (29), respectively. Note that $\boldsymbol{m}^{\mathsf{D}}$ is a gradient diffusion term with spatially dependent diffusion coefficient and that $\boldsymbol{l}$ has contributions from vortex transport ($\boldsymbol{l}^{\mathsf{C}}$) and stretching ($\boldsymbol{l}^{\mathsf{S}}$). Meanwhile, $\boldsymbol{m}^{\mathsf{Z}}$ is a generalized transport term involving spatial gradients of vorticity and eddy diffusivity.

In estimating $\boldsymbol{m}^{\mathsf{D}}$, we rely on the Lagrangian approximations developed by Degond and Mas-Gallic [43] for an isotropic, spatially dependent diffusivity. In particular, it is shown in [43] that the gradient diffusion operator $D[\zeta] \equiv \nabla \cdot (b(\boldsymbol{x})\nabla\zeta(\boldsymbol{x}))$ can be approximated as

$$D[\zeta](\boldsymbol{X}_k) \approx \frac{1}{\delta^2} \sum_l dV_l \eta_\delta(\boldsymbol{X}_k - \boldsymbol{X}_l)\mu(\boldsymbol{X}_l, \boldsymbol{X}_k)(\zeta_l - \zeta_k), \tag{47}$$

where $\boldsymbol{X}_l$, dV_l, and ζ_l are the particle positions, volumes, and strengths in the Lagrangian representation of ζ. Here, the kernel η_δ is a rapidly decaying smoothing function that obeys similar conditions as the core function used in the particle representation of the vorticity field. Meanwhile, μ is a symmetric kernel which satisfies [43]

$$\mu(\boldsymbol{x}, \boldsymbol{y}) = \mu(\boldsymbol{y}, \boldsymbol{x}), \quad \mu(\boldsymbol{x}, \boldsymbol{x}) = b(\boldsymbol{x}). \tag{48}$$

In the present application of Eq. (47), the kernel η is related to the gradient of the core smoothing function; we use [43]

$$\eta(r) \equiv g(r) = -\frac{2}{r}\frac{df}{dr}. \tag{49}$$

In addition, we choose to associate the kernel μ with the geometric mean diffusivity; i.e., we set

$$\mu(\boldsymbol{x}, \boldsymbol{y}) = \sqrt{b(\boldsymbol{x})b(\boldsymbol{y})}. \tag{50}$$

Another well-known choice for μ is the arithmetic mean, $\mu(\boldsymbol{x}, \boldsymbol{y}) = (b(\boldsymbol{x}) + b(\boldsymbol{y}))/2$ [43].

Thus, the diffusion term $\nabla \cdot (|\tilde{\mathbf{S}}|\nabla\tilde{\omega})$ is approximated using

$$\nabla \cdot (|\tilde{\mathbf{S}}|\nabla\tilde{\omega})_i \approx \frac{1}{\delta^2} \sum_{j=1}^{N} \sqrt{|\tilde{\mathbf{S}}(\boldsymbol{X}_i)||\tilde{\mathbf{S}}(\boldsymbol{X}_j)|}(\tilde{\omega}(\boldsymbol{X}_j) - \tilde{\omega}(\boldsymbol{X}_i))\, dV_j g_\delta(\boldsymbol{X}_j - \boldsymbol{X}_i). \tag{51}$$

Once the diffusion term is obtained at all the particle locations, it is test-filtered according to

$$\overline{\nabla \cdot (|\tilde{\mathbf{S}}|\nabla\tilde{\omega})}(\boldsymbol{X}_i) = \frac{\sum_{j=1}^{N} \nabla \cdot (|\tilde{\mathbf{S}}|\nabla\tilde{\omega})(\boldsymbol{X}_j) \exp\left[-(c|\boldsymbol{X}_i - \boldsymbol{X}_j|/\Delta')^3\right]}{\sum_{j=1}^{N} \exp\left[-(c|\boldsymbol{X}_i - \boldsymbol{X}_j|/\Delta')^3\right]}. \tag{52}$$

A similar approach is adopted for the second term in Eq. (28) which involves diffusion of the test-filtered vorticity. Specifically, Eq. (47) is once again used, in conjunction with the

test filtered vorticity $\bar{\tilde{\omega}}$ and strain $\bar{\tilde{\mathbf{S}}}$; this yields

$$\nabla \cdot (|\bar{\tilde{\mathbf{S}}}|\nabla\bar{\tilde{\omega}})(\boldsymbol{X}_i) \approx \frac{1}{\delta^2}\sum_{j=1}^{N}\sqrt{|\bar{\tilde{\mathbf{S}}}(\boldsymbol{X}_i)||\bar{\tilde{\mathbf{S}}}(\boldsymbol{X}_j)|}(\bar{\tilde{\omega}}(\boldsymbol{X}_j) - \bar{\tilde{\omega}}(\boldsymbol{X}_i))\, dV_j g_\delta(\boldsymbol{X}_j - \boldsymbol{X}_i). \quad (53)$$

The filtered strain and vorticity values are computed by first calculating the filtered velocity gradient, $\nabla\tilde{\boldsymbol{u}}$; this is accomplished by analytically differentiating the desingularized Biot–Savart law and evaluating the resulting expression [44]. The results are then used to compute a test-filtered version of the velocity gradient, as described in Eq. (46). The test filtered vorticity $\bar{\tilde{\omega}}$ and strain $\bar{\tilde{\mathbf{S}}}$ are then extracted from the test filtered velocity gradient using their basic definitions.

We now turn our attention to the evaluation of $\boldsymbol{l}^{\mathsf{C}}$. As mentioned earlier (see Eq. (25)), $\boldsymbol{l}^{\mathsf{C}}$ is a difference between filtered versions of the convective derivative of vorticity, which is absorbed by the Lagrangian formulation. In order to avoid explicit estimates of the vorticity gradient, we first rewrite $\boldsymbol{l}^{\mathsf{C}}$ using the relationship

$$\begin{aligned}\boldsymbol{l}^{\mathsf{C}} &= \overline{\tilde{\boldsymbol{u}}\cdot\nabla\tilde{\omega}} - \bar{\tilde{\boldsymbol{u}}}\cdot\nabla\bar{\tilde{\omega}} \\ &= \left(\frac{\overline{\partial\tilde{\omega}}}{\partial t} + \overline{\tilde{\boldsymbol{u}}\cdot\nabla\tilde{\omega}}\right) - \left(\frac{\partial\bar{\tilde{\omega}}}{\partial t} + \bar{\tilde{\boldsymbol{u}}}\cdot\nabla\bar{\tilde{\omega}}\right) \\ &= \frac{\overline{\tilde{d}\tilde{\omega}}}{dt} - \frac{\bar{\tilde{d}}\bar{\tilde{\omega}}}{dt},\end{aligned} \quad (54)$$

where $\tilde{d}/dt$ represents the time rate of change for an observer moving at $\tilde{\boldsymbol{u}}$ while $\bar{\tilde{d}}/dt$ represents the time rate of change for an observer moving at $\bar{\tilde{\boldsymbol{u}}}$. In the proposed scheme, the filtered Lagrangian derivatives are approximated using a forward derivative:

$$\left[\frac{\tilde{d}\tilde{\omega}}{dt}\right](\boldsymbol{X}_i, t) \approx \frac{\tilde{\omega}(\boldsymbol{X}_i(t+\Delta t), t+\Delta t) - \tilde{\omega}(\boldsymbol{X}_i(t), t)}{\Delta t} \quad (55)$$

and

$$\left[\frac{\bar{\tilde{d}}\bar{\tilde{\omega}}}{dt}\right](\boldsymbol{X}_i, t) \approx \frac{\bar{\tilde{\omega}}(\boldsymbol{X}_i(t) + \Delta t\bar{\tilde{\boldsymbol{u}}}_i(t), t+\Delta t) - \bar{\tilde{\omega}}(\boldsymbol{X}_i(t), t)}{\Delta t}. \quad (56)$$

Based on the above approximations, we are now in a position to estimate $\boldsymbol{m}^{\mathsf{D}}$ and $\boldsymbol{l}^{\mathsf{C}}$ for each element directly from the Lagrangian data. Evaluation of $\boldsymbol{l}^{\mathsf{S}}$ can be performed directly, based on the computed values of the stretching term. However, *a priori* tests performed in the following section show that, for the purpose of evaluating C_r, $\boldsymbol{l}^{\mathsf{S}}$ can be safely neglected. The tests show that $\boldsymbol{m}^{\mathsf{Z}}$ can be omitted as well, and this is a significant advantage since its evaluation is generally cumbersome.

Taking advantage of these results, we can now proceed directly to the evaluation of C_r. As shown in Eq. (31), C_r is given in terms of spatial averages of $\boldsymbol{l}\cdot\boldsymbol{m}$ and $\boldsymbol{m}\cdot\boldsymbol{m}$. In the Lagrangian computations, these averages are computed by direct summation over the fields of the elements; we use

$$\langle \boldsymbol{l}\cdot\boldsymbol{m}\rangle = \frac{\sum_{i=1}^{N}\boldsymbol{l}_i\cdot\boldsymbol{m}_i\, dV_i}{\sum_{i=1}^{N} dV_i}, \quad (57)$$

$$\langle \boldsymbol{m} \cdot \boldsymbol{m} \rangle = \frac{\sum_{i=1}^{N} \boldsymbol{m}_i \cdot \boldsymbol{m}_i \, dV_i}{\sum_{i=1}^{N} dV_i}. \tag{58}$$

The model coefficient is then obtained from

$$C_r^2 = \frac{\sum_{i=1}^{N} \boldsymbol{l}_i \cdot \boldsymbol{m}_i \, dV_i}{\sum_{i=1}^{N} \boldsymbol{m}_i \cdot \boldsymbol{m}_i \, dV_i}. \tag{59}$$

4. A PRIORI TESTS OF SFS MODEL

In this section, the basic properties of the SFS model are examined through *a priori* tests, using data from direct numerical simulations (DNS) of homogeneous, isotropic turbulence. The DNS data resulting from these simulations can provide direct estimates of the "real" SFS torque. The resulting data can then be used to assess the performance of the SFS model. The analysis aims at addressing a variety of fundamental questions regarding both the real and modeled SFS torques, including: (1) What is the relative importance of SFS stretching and tilting compared with SFS convection?; (2) How important is the "nondiffusive" part of the torque model?; (3) How well aligned are the real and modeled SFS torques?; (4) How does the dynamic model coefficient compare with the theoretical value?; etc. These questions are tackled below, following a brief description of the DNS data.

4.1. *DNS Data*

The DNS data used in the present work were obtained from simulations of forced, isotropic turbulence [45]. The simulations were performed using a pseudo-spectral discretization of the Navier–Stokes equations in rotation form. Time integration is based on exact factorization of the viscous term and second-order Adams–Bashforth treatment of the nonlinear term. Thus, the solution is advanced according to [46, 47],

$$\hat{\boldsymbol{u}}^{n+1} = \hat{\boldsymbol{u}}^n \exp(-\nu k^2 \Delta t) + \Delta t \mathbf{P} \cdot \left[\frac{3}{2} \widehat{(\boldsymbol{u} \times \boldsymbol{\omega})}^n \exp(-\nu k^2 \Delta t) - \frac{1}{2} \widehat{(\boldsymbol{u} \times \boldsymbol{\omega})}^{n-1} \exp(-2\nu k^2 \Delta t) + \hat{\boldsymbol{f}}^n \exp(-\nu k^2 \Delta t) \right], \tag{60}$$

where $\mathbf{P}$ is the projection operator in the direction perpendicular to wavenumber vector $\boldsymbol{k}$, $k \equiv |\boldsymbol{k}|$, and Δt is the time step. The forcing $\hat{\boldsymbol{f}}$ is adjusted at every time step to maintain a constant energy injection rate. Forcing is performed for low wave numbers falling within the sphere $0 < |\boldsymbol{k}| < 2$; it is expressed as

$$\hat{\boldsymbol{f}}_{\boldsymbol{k}} = \epsilon \frac{\hat{\boldsymbol{u}}_{\boldsymbol{k}}}{\sum_{0<|\boldsymbol{k}|<2} \hat{\boldsymbol{u}}_{\boldsymbol{k}} \cdot \hat{\boldsymbol{u}}_{\boldsymbol{k}}}, \tag{61}$$

where ϵ is the energy injection rate. Dealiasing of quadratic terms is found to be unnecessary for this well-resolved DNS, but a spherical truncation procedure is nevertheless implemented.

Table I summarizes parameters used in the simulations. There are essentially two data sets with different resolutions, both at moderate, Reynolds number. We will primarily rely on the larger data set with $N = 128^3$ grid points.

TABLE I
DNS Simulation Parameters

N	64	128
L	2π	2π
u'	0.11	0.22
ℓ	1.37	1.33
λ	0.56	0.42
Re_λ	66	93
ϵ	0.000704	0.004
η	0.0345	0.0224
ν	0.001	0.001

Note. L is the domain length, N^3 is the number of points, u' is the root-mean-square velocity, ℓ is the integral scale, λ is the Taylor microscale, Re_λ is the Taylor Reynolds number, ϵ is the energy injection (and average dissipation) rate, η is the Kolmogrov scale, and ν is the kinematic viscosity.

4.2. *Decomposition of Real and Modeled SFS Torques*

Following the discussion in Section 2 the real SFS torque, $\boldsymbol{r}$, has contributions from SFS convection and SFS stretching and tilting. We identify these contributions by decomposing $\boldsymbol{r}$ using

$$r_i = r_i^{\mathsf{C}} + r_i^{\mathsf{S}}, \tag{62}$$

where

$$r_i^{\mathsf{C}} \equiv -\frac{\partial}{\partial x_j}(\widetilde{\omega_i u_j} - \tilde{\omega}_i \tilde{u}_j) \tag{63}$$

and

$$r_i^{\mathsf{S}} \equiv \frac{\partial}{\partial x_j}(\widetilde{u_i \omega_j} - \tilde{u}_i \tilde{\omega}_j). \tag{64}$$

Thus, $\boldsymbol{r}^{\mathsf{C}}$ and $\boldsymbol{r}^{\mathsf{S}}$, respectively, denote the contribution of SFS transport and SFS stretching and tilting to the overall SFS torque $\boldsymbol{r}$.

In large-eddy simulations $\boldsymbol{r}$ is not known and so it is replaced with the SFS model $\boldsymbol{g}$ (Eq. (15)). The latter is also decomposed into two parts,

$$g_i = g_i^{\mathsf{D}} + g_i^{\mathsf{Z}}, \tag{65}$$

where

$$g_i^{\mathsf{D}} \equiv C_r^2 \Delta^2 \frac{\partial}{\partial x_j}\left(\sqrt{2\tilde{\mathsf{S}}_{mn}\tilde{\mathsf{S}}_{mn}}\frac{\partial \tilde{\omega}_i}{\partial x_j}\right) \tag{66}$$

is a familiar gradient-diffusion term, and

$$g_i^{\mathsf{Z}} \equiv -C_r^2 \Delta^2 \frac{\partial}{\partial x_j}\left(\sqrt{2\tilde{\mathsf{S}}_{mn}\tilde{\mathsf{S}}_{mn}}\right)\frac{\partial \tilde{\omega}_j}{\partial x_i} \tag{67}$$

is an additional term due to spatially varying eddy viscosity.

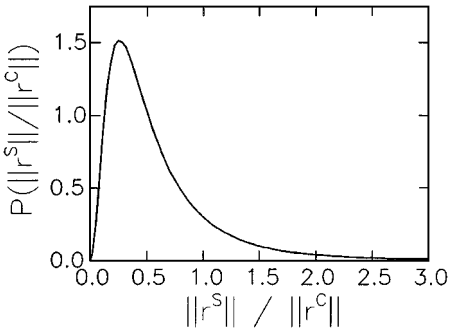

FIG. 2. Probability density of $\|\boldsymbol{r}^{\mathsf{C}}\|/\|\boldsymbol{r}^{\mathsf{S}}\|$.

Below, we examine the behavior of $\boldsymbol{r}$ and assess the roles of SFS transport ($\boldsymbol{r}^{\mathsf{C}}$) and SFS stretching and tilting ($\boldsymbol{r}^{\mathsf{S}}$). Similarly, we examine the relative contributions of $\boldsymbol{g}^{\mathsf{D}}$ and $\boldsymbol{g}^{\mathsf{Z}}$ to the modeled SFS torque $\boldsymbol{g}$. Insight gained from this exercise is used to guide analysis of model performance.

4.3. *Roles of SFS Convection and SFS Stretching and Tilting*

The relative magnitudes of $\boldsymbol{r}^{\mathsf{C}}$ and $\boldsymbol{r}^{\mathsf{S}}$ are examined using the 128^3 DNS data set. The filter width is set to $\Delta = 0.448$, which corresponds to 11 mesh spacings approximately. The ratios of filter width to Kolmogorov scale and filter width to integral scale are $\Delta/\eta = 20$ and $\Delta/\ell = 0.34$, respectively. Filtering of the DNS data is performed using the third-order Gaussian filter (Eq. (43)).

Figure 2 shows the probability density distribution of the ratio of torque magnitudes $\|\boldsymbol{r}^{\mathsf{S}}\|/\|\boldsymbol{r}^{\mathsf{C}}\|$. The figure shows that $\boldsymbol{r}^{\mathsf{S}}$ is generally smaller than $\boldsymbol{r}^{\mathsf{C}}$, but that it is not negligible. In fact, the results in Fig. 2 indicate that the magnitude of $\boldsymbol{r}^{\mathsf{S}}$ is larger than that of $\boldsymbol{r}^{\mathsf{C}}$ in over 15% of the volume of the flow. Table II shows the magnitudes of the subfilter scale torques $\boldsymbol{r}^{\mathsf{C}}$ and $\boldsymbol{r}^{\mathsf{S}}$ conditionally averaged over those regions where $\|\boldsymbol{r}^{\mathsf{C}}\| > \|\boldsymbol{r}^{\mathsf{S}}\|$, and where $\|\boldsymbol{r}^{\mathsf{C}}\| \le \|\boldsymbol{r}^{\mathsf{S}}\|$. Also shown are the averaged values over the entire domain. The results show that the ratio of the average magnitude of $\boldsymbol{r}^{\mathsf{C}}$ and $\boldsymbol{r}^{\mathsf{S}}$ in the entire domain is $\langle\|\boldsymbol{r}^{\mathsf{S}}\|\rangle/\langle\|\boldsymbol{r}^{\mathsf{C}}\|\rangle = 0.456$. Table II also indicates that, where $\|\boldsymbol{r}^{\mathsf{S}}\|$ exceeds $\|\boldsymbol{r}^{\mathsf{C}}\|$, it is as much due to $\|\boldsymbol{r}^{\mathsf{S}}\|$ being large as it is due to $\|\boldsymbol{r}^{\mathsf{C}}\|$ being small; i.e., large values of $\|\boldsymbol{r}^{\mathsf{S}}\|/\|\boldsymbol{r}^{\mathsf{C}}\|$ do not occur only where $\|\boldsymbol{r}^{\mathsf{C}}\|$ is unusually small.

Table III provides the correlation coefficient between the two SFS torques $\boldsymbol{r}^{\mathsf{C}}$ and $\boldsymbol{r}^{\mathsf{S}}$. Included is a breakdown of the results into quintiles of magnitudes of $\boldsymbol{r}^{\mathsf{C}}$ and of $\boldsymbol{r}^{\mathsf{S}}$. The breakdown is based on defining five bins each associated with an interval of torque

TABLE II
Averages and Conditional Averages of Normalized Subfilter Scale Torques

$\cdot$	$\langle\|\cdot\|\rangle$	$\langle\|\cdot\|\|\|\boldsymbol{r}^{\mathsf{C}}\| > \|\boldsymbol{r}^{\mathsf{S}}\|\rangle$	$\langle\|\cdot\|\|\|\boldsymbol{r}^{\mathsf{C}}\| \le \|\boldsymbol{r}^{\mathsf{S}}\|\rangle$
$\boldsymbol{r}^{\mathsf{C}}$	11.8	14.0	6.14
$\boldsymbol{r}^{\mathsf{S}}$	5.83	5.26	8.99

Note. Values of $\boldsymbol{r}^{\mathsf{C}}$ and $\boldsymbol{r}^{\mathsf{S}}$ are normalized by multiplying by ℓ^2/u'^2.

TABLE III
Correlation of r^C and r^S

Quintile		Correlation		Correlation
All	$\|r^C\|$	−0.276	$\|r^S\|$	−0.276
0	0.0668		0.0093	
1	5.06	−0.0956	2.25	−0.0713
2	8.15	−0.148	3.65	−0.118
3	12.0	−0.189	5.43	−0.163
4	18.7	−0.238	8.50	−0.218
5	141.	−0.345	68.4	−0.364

Note. The correlation coefficient is $\langle r^C \cdot r^S \rangle / [\langle r^C \cdot r^C \rangle \langle r^S \cdot r^S \rangle]^{1/2}$. The columns $\|r^C\|$ and $\|r^S\|$ contain the ith quintile of those norms. The zeroth quintile value is the lowest value of the corresponding norm. The correlation value for the ith quintile is the correlation value obtained using the set of points where the norm falls between values indicated at rows i and $i-1$.

magnitudes; each bin contains those data points where the torque magnitude falls within the associated interval. These intervals form a partition of the overall range of torque magnitudes, and their endpoints are selected so that each bin contains essentially the same number of points. Thus, when the data is binned according to the magnitude of r^C, the first bin contains those points for which $\|r^C\|$ falls within the first quintile, the second bin contains points for which $\|r^C\|$ is within the second quintile, and so on. The results in Table III show that r^C and r^S have a small tendency to be anticorrelated. This result is also illustrated in Fig. 3 which depicts the distribution of the angle between r^C and r^S. Also plotted using a dotted line is a sine curve, which corresponds to a uniform random distribution of angles. The data in Fig. 3 are shifted to the right of the dotted line, indicating a propensity for r^C and r^S to be anti-aligned. The correlation values in Table III show that anti-alignment is more likely for larger vectors, while small vectors are almost randomly aligned.

One can conclude from the present analysis of the real SFS torque that the effects of subfilter scale convection and of subfilter scale stretching and tilting are both significant and that, in principle, an accurate model should reproduce both effects. The results show that r^C and r^S follow different trends and may thus require different models.

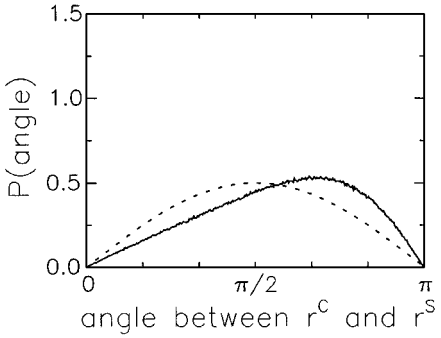

FIG. 3. Probability density of the angle between r^C and r^S. The dotted line follows a sine function distribution, which would correspond to uniform random alignment between the two torques.

TABLE IV
Averages and Conditional Averages of Normalized Model Subfilter Scale Torques

$\cdot$	$\langle \|\cdot/C_r^2\| \rangle$	$\langle \|\cdot/C_r^2\| \mid \|\boldsymbol{g}^{\mathrm{D}}\| > \|\boldsymbol{g}^{\mathrm{Z}}\| \rangle$	$\langle \|\cdot/C_r^2\| \mid \|\boldsymbol{g}^{\mathrm{D}}\| \le \|\boldsymbol{g}^{\mathrm{Z}}\| \rangle$
$\boldsymbol{g}^{\mathrm{D}}$	849.	860.	167.
$\boldsymbol{g}^{\mathrm{Z}}$	110.	108.	232.

Note. Values of $\boldsymbol{g}^{\mathrm{D}}$ and $\boldsymbol{g}^{\mathrm{Z}}$ are normalized by multiplying by ℓ^2/u'^2.

4.4. *Behavior of SFS Model*

A similar analysis is conducted for the modeled SFS torques $\boldsymbol{g}^{\mathrm{D}}$ and $\boldsymbol{g}^{\mathrm{Z}}$. Figure 4 shows the distribution of the ratio $\|\boldsymbol{g}^{\mathrm{Z}}\|/\|\boldsymbol{g}^{\mathrm{D}}\|$. The curve shows that $\boldsymbol{g}^{\mathrm{Z}}$ is typically an order of magnitude smaller than $\boldsymbol{g}^{\mathrm{D}}$. It also indicates that the magnitude of $\boldsymbol{g}^{\mathrm{Z}}$ exceeds that of $\boldsymbol{g}^{\mathrm{D}}$ in less than 1.5% of the volume of the domain.

These observations are further amplified in Table IV, which provides averages and conditional averages of $\|\boldsymbol{g}^{\mathrm{Z}}\|$ and $\|\boldsymbol{g}^{\mathrm{D}}\|$. Consistent with the trends in Fig. 4, Table IV shows that the ratio of the average magnitudes of $\boldsymbol{g}^{\mathrm{Z}}$ and $\boldsymbol{g}^{\mathrm{D}}$ is quite small; $\langle\|\boldsymbol{g}^{\mathrm{Z}}\|\rangle/\langle\|\boldsymbol{g}^{\mathrm{D}}\|\rangle = 0.130$. In addition, the tabulated conditional averages indicate that where the ratio $\|\boldsymbol{g}^{\mathrm{Z}}\|/\|\boldsymbol{g}^{\mathrm{D}}\|$ is large, it is primarily due to small values of $\|\boldsymbol{g}^{\mathrm{D}}\|$. Finally, Table V shows that $\boldsymbol{g}^{\mathrm{D}}$ and $\boldsymbol{g}^{\mathrm{Z}}$ are poorly correlated, with near-zero correlation at all bands of $\|\boldsymbol{g}^{\mathrm{D}}\|$ and $\|\boldsymbol{g}^{\mathrm{Z}}\|$. This is also illustrated in Fig. 5, which shows that the angle between the two SFS torques nearly follows a random distribution.

The present tests clearly indicate that $\boldsymbol{g}^{\mathrm{Z}}$ plays a minor role in the SFS model. Moreover, since its evaluation in the context of a particle approximation would be quite involved, we will assume that $\boldsymbol{g}^{\mathrm{Z}}$ can be neglected from the model. This approximation will be adopted in the tests of the following section and implemented in [14].

4.5. *Correlation of* $\boldsymbol{r}$ *and* $\boldsymbol{g}$

In this section the modeled subfilter scale torque $\boldsymbol{g}$ is compared to the "real" SFS torque $\boldsymbol{r}$. The analysis relies on the same data set and parameters used in the previous section.

Figure 6 shows the distribution of relative orientation of the SFS torques $\boldsymbol{r}$ and $\boldsymbol{g}$. Plotted are five curves corresponding to a breakdown of the data into quintiles of $\|\boldsymbol{r}\|$. Ideally, the

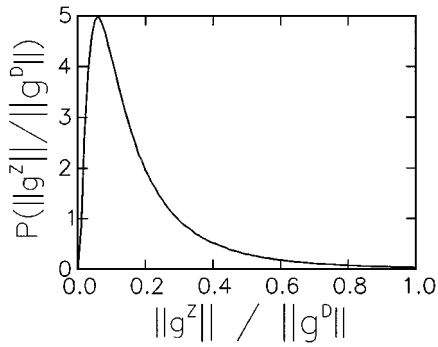

FIG. 4. Distribution of the ratio $\|\boldsymbol{g}^{\mathrm{Z}}\|/\|\boldsymbol{g}^{\mathrm{D}}\|$.

TABLE V
Correlation of g^D and g^Z. The correlation coefficient is $\langle g^D \cdot g^Z \rangle / [\langle g^D \cdot g^D \rangle \langle g^Z \cdot g^Z \rangle]^{1/2}$

Quintile All		Correlation		Correlation
	$\|g^D/C_r^2\|$	0.00600	$\|g^Z/C_r^2\|$	0.00600
0	2.80		0.252	
1	308.	0.00404	37.5	0.00437
2	515.	0.0113	64.9	0.000366
3	788.	0.0126	101.	−0.000671
4	1250	0.0123	163.	0.000168
5	9160	0.0028	1830	0.0110

Note. A breakdown into quintiles is performed as in Table III.

modeled torque would be perfectly aligned with the real torque, and the angle between the two vectors would be everywhere equal to zero. Figure 6 shows that the alignment between $\boldsymbol{r}$ and $\boldsymbol{g}$ is substantial, although far from perfect. It is interesting to note that the alignment is strongest where $\|\boldsymbol{r}\|$ is largest. This exercise was repeated by breaking down the data according to the magnitude of $\|\boldsymbol{g}\|$; the results reveal essentially the same trends as those shown in Fig. 6 and are therefore omitted. On the other hand, the results show a different trend when binning is based on the magnitude of the resolved vorticity $\|\tilde{\boldsymbol{\omega}}\|$. Figure 7 shows that the alignment between $\boldsymbol{r}$ and $\boldsymbol{g}$ is almost independent of vorticity magnitude.

Tables VI and VII provide correlation coefficients and conditional correlations of $\boldsymbol{r}$ and $\boldsymbol{g}$. The results show that correlation of $\boldsymbol{r}$ and $\boldsymbol{g}$ is around 0.6 in the highest quintile of $\|\boldsymbol{r}\|$ but only around 0.2 in the lowest quintile of $\|\boldsymbol{r}\|$ (Table VI). In contrast, when binning is based on $\|\tilde{\boldsymbol{\omega}}\|$, Table VII shows that the correlation of $\boldsymbol{r}$ and $\boldsymbol{g}$ varies slightly, from 0.573 for the highest quintile to 0.444 for the lowest quintile.

One concern in *a priori* tests is that too much information may be used to calculate the subfilter scale torque model $\boldsymbol{g}$, information that would not be available at the resolved scales during LES (see the discussion in Liu *et al.* [22]). To examine this issue the spectral collocation approximation of $\boldsymbol{g}$ is replaced with its centered-difference approximation on meshes coarser than that of the DNS. Tables VI and VII provide correlation results obtained from both a spectral collocation approximation on the DNS grid (mesh size h), and

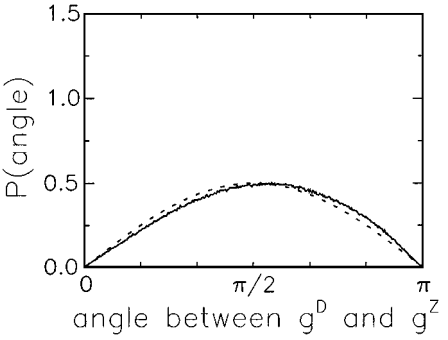

FIG. 5. Alignment of g^D and g^Z.

TABLE VI
Correlation of *r* and *g*

Quintile		Spectral	Finite difference $\Delta_{FD}/\Delta_{filter}$ 0.0867	0.173	0.260	0.347
		Correlation coefficients				
All	$\|\boldsymbol{r}\| \times \ell^2/u'^2$	0.513	0.453	0.451	0.419	0.359
0	0.0436					
1	5.32	0.173	0.153	0.155	0.147	0.125
2	8.35	0.269	0.238	0.240	0.226	0.194
3	12.1	0.352	0.311	0.313	0.295	0.253
4	18.4	0.440	0.392	0.394	0.372	0.324
5	147.	0.611	0.541	0.540	0.509	0.450

Note. The correlation coefficient is $\langle \boldsymbol{r}\cdot\boldsymbol{g}\rangle/[\langle \boldsymbol{r}\cdot\boldsymbol{r}\rangle\langle \boldsymbol{g}\cdot\boldsymbol{g}\rangle]^{1/2}$. A breakdown into quintiles of $\|\boldsymbol{r}\|$ is performed, as in Table III. $\Delta_{FD}/\Delta_{filter}$ gives the ratio of the finite-difference grid to the filter width.

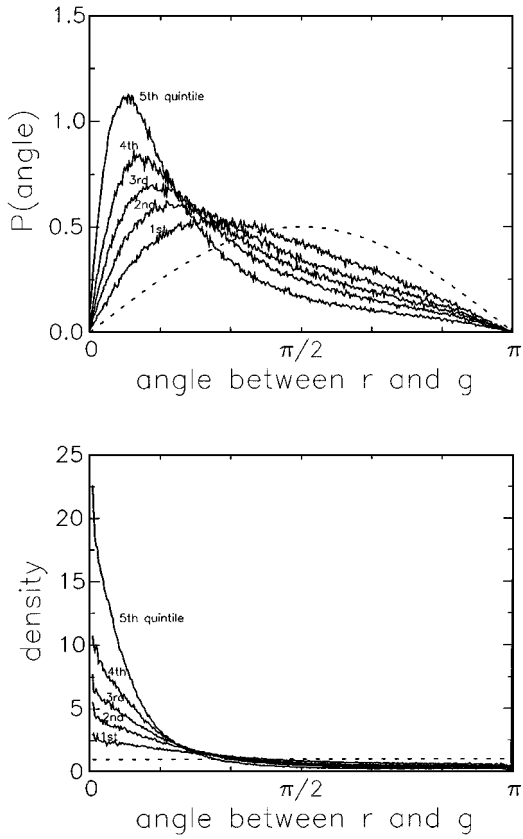

FIG. 6. Alignment of real and modeled SFS torques, binned by quintiles of $\|\boldsymbol{r}\|$: (top) distribution of the angle between $\boldsymbol{r}$ and $\boldsymbol{g}$; (bottom) relative density.

TABLE VII
Correlation of *r* and *g*

			Finite difference $\Delta_{FD}/\Delta_{filter}$			
		Spectral	0.0867	0.173	0.260	0.347
Quintile		Correlation coefficients				
All	$\|\tilde{\omega}\| \times \ell/u'$	0.513	0.453	0.451	0.419	0.359
0	0.0336					
1	2.92	0.444	0.375	0.370	0.325	0.237
2	4.40	0.466	0.395	0.392	0.351	0.272
3	6.06	0.498	0.423	0.420	0.383	0.314
4	8.40	0.530	0.463	0.462	0.429	0.367
5	28.1	0.573	0.521	0.520	0.496	0.452

Note. The correlation coefficient is $\langle \boldsymbol{r}\cdot\boldsymbol{g}\rangle/[\langle \boldsymbol{r}\cdot\boldsymbol{r}\rangle\langle \boldsymbol{g}\cdot\boldsymbol{g}\rangle]^{1/2}$. A breakdown into quintiles of $\|\tilde{\omega}\|$ is performed, as in Table III. $\Delta_{FD}/\Delta_{filter}$ gives the ratio of the finite-difference grid to the filter width.

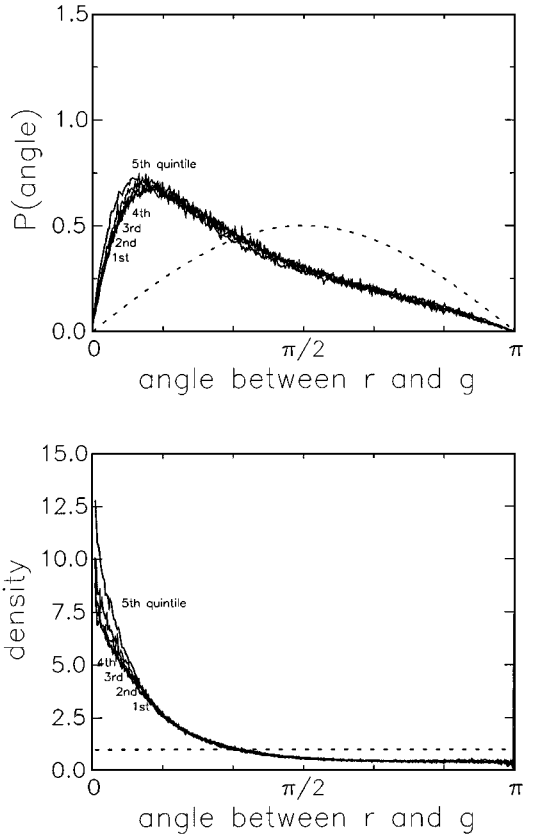

FIG. 7. Alignment of real and modeled SFS torques, binned by quintiles of $\|\tilde{\omega}\|$: (top) distribution of the angle between $\boldsymbol{r}$ and $\boldsymbol{g}$; (bottom) relative density.

second-order centered differences on regular grids of mesh size $\Delta x = h, 2h, 3h$, and $4h$. Recall that the filter size Δ is roughly $11h$. As a reference, typical particle spacings to be employed in Lagrangian simulations [14] are half the core size, i.e. $\Delta/(2c) \sim 2h$.

At $\Delta x = h$, the correlations obtained with finite differences are about 11% lower than those obtained using the spectral computations. This drop could be attributed to lower accuracy in the finite difference calculations, but not to filtering or loss of information since the same data set is fed to both calculations. The correlation results are nearly the same when using centered differences with $\Delta x = h$ and $\Delta x = 2h$. This indicates that the quantities being evaluated are smooth at those scales. However, as Δx is increased further the correlation of $\boldsymbol{r}$ and $\boldsymbol{g}$ once again decreases; at $\Delta x = 4h$ the correlation is about 27% smaller than the spectral prediction. The drop in correlation is quite even across all quintiles of $\|\boldsymbol{r}\|$. On the other hand, when binning is based on resolved vorticity magnitude the drop in correlation is smaller where $\|\tilde{\boldsymbol{\omega}}\|$ is high, and greater where $\|\tilde{\boldsymbol{\omega}}\|$ is low.

The alignment between $\boldsymbol{g}$ and $\boldsymbol{r}$ is also examined by binning the data according to the enstrophy source term $\tilde{\boldsymbol{\omega}} \cdot \boldsymbol{r}$ and $\tilde{\boldsymbol{\omega}} \cdot \boldsymbol{g}$. These terms represent production or dissipation of resolved enstrophy by the real and modeled SFS torques, respectively. Figure 8 shows that alignment of $\boldsymbol{r}$ and $\boldsymbol{g}$ is highest where $\tilde{\boldsymbol{\omega}} \cdot \boldsymbol{r}$ is smallest (most negative). (Results obtained by binning according to $\tilde{\boldsymbol{\omega}} \cdot \boldsymbol{g}$ show a similar trend and are omitted.) In other words, where the real subfilter torque is diminishing the resolved enstrophy, it acts in a diffusive fashion.

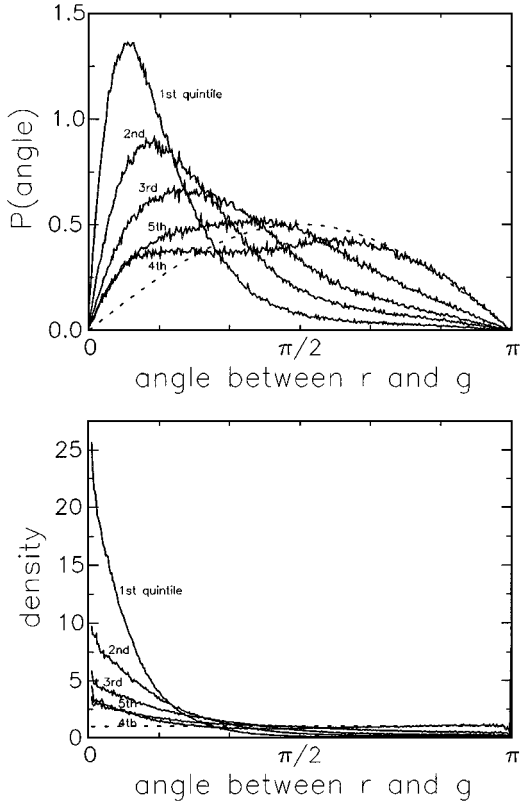

FIG. 8. Alignment of real and modeled SFS torques, binned by quintiles of $\tilde{\boldsymbol{\omega}} \cdot \boldsymbol{r}$: (top) distribution of the angle between $\boldsymbol{r}$ and $\boldsymbol{g}$; (bottom) relative density.

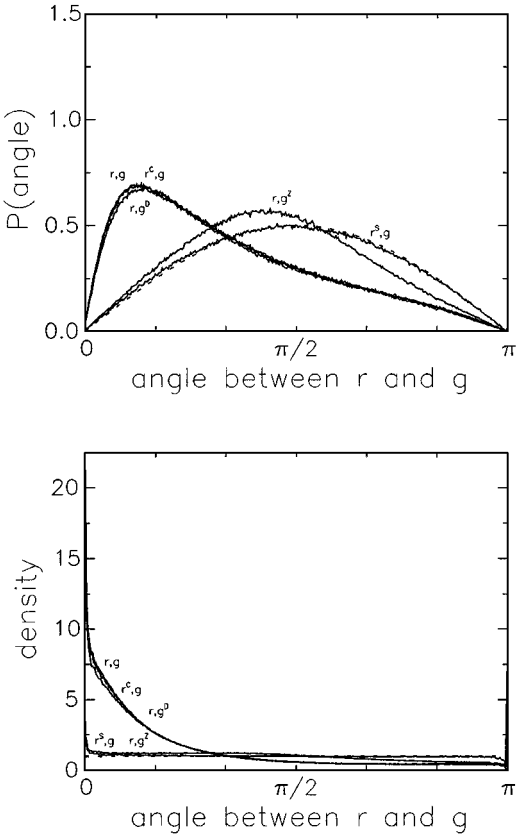

FIG. 9. Alignment of portions of the real and modeled SFS torques.

In order to gain deeper insight into the strengths and weaknesses of the model, we analyze the correlation of only portions of the SFS torque and the SFS model, e.g. $\boldsymbol{r}^{\mathrm{C}}$ versus $\boldsymbol{g}$, or $\boldsymbol{r}$ versus $\boldsymbol{g}^{\mathrm{Z}}$. Results of this exercise are plotted in Fig. 9. The alignments of $\boldsymbol{r}$ and $\boldsymbol{g}^{\mathrm{D}}$ and of $\boldsymbol{r}^{\mathrm{C}}$ and $\boldsymbol{g}$ have distributions which are similar to that of $\boldsymbol{r}$ and $\boldsymbol{g}$. On the other hand, the relative orientations of $\boldsymbol{r}$ and $\boldsymbol{g}^{\mathrm{Z}}$ show no preferred alignment; $\boldsymbol{r}^{\mathrm{S}}$ and $\boldsymbol{g}$ show a slight tendency to form a 70° angle, but their alignment is basically random. Figure 9 indicates that the partial alignment of $\boldsymbol{r}$ and $\boldsymbol{g}$ is primarily due to the correlation between $\boldsymbol{r}^{\mathrm{C}}$ and $\boldsymbol{g}^{\mathrm{D}}$. There is no relation between $\boldsymbol{r}$ and $\boldsymbol{g}^{\mathrm{Z}}$, nor between $\boldsymbol{r}^{\mathrm{S}}$ and $\boldsymbol{g}^{\mathrm{D}}$. These observations provide additional motivation for ignoring $\boldsymbol{g}^{\mathrm{Z}}$. However, it was shown above that SFS stretching is significant, so that the poor alignment between $\boldsymbol{g}$ and $\boldsymbol{r}^{\mathrm{S}}$ is clearly a weakness of the model.

Briefly, the indications from the present analysis are that the diffusive SFS torque model has some correlation with the convective portion of the SFS torque but that it does not do anything to capture the effects of SFS vortex stretching and tilting. An effective model of the subfilter scale stretching and tilting would be a significant addition to the model used in the present work, but this problem is relegated for future work in this area. While yielding low correlation coefficients during *a priori* tests, the eddy–viscosity closure still has advantages from a practical point of view, mainly because it enhances numerical stability and dissipation. The main practical difficulty with this model is to choose the model coefficient, which we address in the next sections.

4.6. *Determination of Model Coefficient*

The correlations of $\boldsymbol{r}$ and $\boldsymbol{g}$ obtained in the previous section, as well as the corresponding alignment angles, are independent of the value of the model coefficient, C_r. For the subfilter scale model to be complete, however, C_r must be determined. In this section, we explore three methods for computing C_r. They are all based on the L_2 norm appropriate to the present formalism, the enstrophy being defined as $\frac{1}{2}\langle\tilde{\omega}_i\tilde{\omega}_i\rangle$. As detailed in Appendix A, the resolved enstrophy is produced by resolved vortex stretching and dissipated by the subfilter terms.

In the first and second approaches, we rely on the DNS data to determine the value of the model coefficient. The first approach is based directly on the balance between enstrophy production and modeled enstrophy dissipation by the model:

$$\langle\tilde{\omega}_i\tilde{\omega}_j\tilde{\mathsf{S}}_{ij}\rangle = \nu\left\langle\frac{\partial\tilde{\omega}_i}{\partial x_j}\frac{\partial\tilde{\omega}_i}{\partial x_j}\right\rangle + C_r^2\Delta^2\left\langle\sqrt{2\tilde{\mathsf{S}}_{mn}\tilde{\mathsf{S}}_{mn}}\frac{\partial\tilde{\omega}_i}{\partial x_j}\frac{\partial\tilde{\omega}_i}{\partial x_j}\right\rangle + C_r^2\Delta^2\left\langle\frac{\partial}{\partial x_j}\left(\sqrt{2\tilde{\mathsf{S}}_{mn}\tilde{\mathsf{S}}_{mn}}\right)\frac{\partial}{\partial x_i}(\tilde{\omega}_i\tilde{\omega}_j)\right\rangle, \tag{68}$$

from which C_r can be immediately determined by evaluating the averages from the DNS. The second approach is similar to the first; it is based on requiring that the SFS model dissipate the same amount of resolved enstrophy as the real SFS torque, i.e. on enforcing the balance

$$\langle\tilde{\boldsymbol{\omega}}\cdot\boldsymbol{r}\rangle = \langle\tilde{\boldsymbol{\omega}}\cdot\boldsymbol{g}\rangle. \tag{69}$$

Substituting the definitions of $\boldsymbol{r}$ and $\boldsymbol{g}$ (Eqs. (62)–(67)) into Eq. (69) yields

$$\left\langle\tilde{\omega}_i\left[-\frac{\partial}{\partial x_j}(\widetilde{\omega_i u_j} - \tilde{\omega}_i\tilde{u}_j) + \frac{\partial}{\partial x_j}(\widetilde{u_i\omega_j} - \tilde{u}_i\tilde{\omega}_j)\right]\right\rangle = C_r^2\left\langle\tilde{\omega}_i\left[\Delta^2\frac{\partial}{\partial x_j}\left(\sqrt{2\tilde{\mathsf{S}}_{mn}\tilde{\mathsf{S}}_{mn}}\frac{\partial\tilde{\omega}_i}{\partial\tilde{x}_j}\right) - \Delta^2\frac{\partial}{\partial x_j}\left(\sqrt{2\tilde{\mathsf{S}}_{mn}\tilde{\mathsf{S}}_{mn}}\right)\frac{\partial\tilde{\omega}_j}{\partial x_i}\right]\right\rangle. \tag{70}$$

Equation (70) can be directly used to compute C_r. Note that, unlike the first method, the unfiltered values, or at least averages of products of unfiltered values, are required. Naturally, these are taken from the unfiltered DNS data.

In the third approach, C_r is evaluated using the dynamic procedure. To this end, the vectors $\boldsymbol{l}$ and $\boldsymbol{m}$ are evaluated from their definitions, i.e. by plugging the filtered data into Eqs. (24)–(29). Once $\boldsymbol{l}$ and $\boldsymbol{m}$ are computed, C_r is determined using Eq. (31).

The predictions of the first method are provided in Table VIII. The results show that the predicted values of C_r for different filter sizes are comparable but that C_r decreases as Δ increases. The drop in C_r is weak when Δ is small, but it is noticeable when Δ approaches the integral scale. Table VIII also provides the average value of enstrophy production and viscous dissipation. The computed values show that at small filter scales the resolved enstrophy is primarily dissipated by molecular viscosity, while at large filter size most of the dissipation is due to SFS torques.

Additional information regarding the enstrophy balance leading to the present predictions is provided in Table IX, which shows the computed values of the remaining terms in Eq. (68).

TABLE VIII
Model Constant C_r Obtained by Balancing Enstrophy Production and Dissipation

Δ/η	N	C_r	$\langle\tilde{\omega}\tilde{\omega} : \tilde{\mathbf{S}}\rangle \times \ell^3/u'^3$	$\nu\langle\nabla\tilde{\omega} : \nabla\tilde{\omega}^{\mathsf{T}}\rangle \times \ell^3/u'^3$
5	128	0.0858	197.64	148.54
10	128	0.0816	112.56	59.024
20	128	0.0772	39.344	12.456
40	128	0.0734	8.7664	1.5396
80	128	0.0591	1.1763	.15265
6.5	64	0.0802	93.198	65.686
13	64	0.0767	44.240	20.855
26	64	0.0702	11.687	3.4655
52	64	0.0601	1.6987	.35335

Note. Results are obtained for different filter sizes, using both the 64^3 and 128^3 DNS data sets.

The results in Table IX support some of the approximations made in the analysis (see Appendix A); in particular they show that

$$\langle(\nabla|\tilde{\mathbf{S}}|)\cdot[\nabla\cdot(\tilde{\omega}\tilde{\omega})]\rangle \ll \langle|\tilde{\mathbf{S}}|\nabla\tilde{\omega} : \nabla\tilde{\omega}^{\mathsf{T}}\rangle \tag{71}$$

and

$$\langle|\tilde{\mathbf{S}}|\nabla\tilde{\omega} : \nabla\tilde{\omega}^{\mathsf{T}}\rangle \approx \langle|\tilde{\mathbf{S}}|\rangle\langle\nabla\tilde{\omega} : \nabla\tilde{\omega}^{\mathsf{T}}\rangle. \tag{72}$$

The predictions of the dynamic model are given in Table X. In all cases considered, the calculations are based on a test filter width $\Delta' = 2\Delta$, as is typically the case in many applications [17]. Included in Table X are calculations made while neglecting $\boldsymbol{I}^{\mathsf{S}}$ and/or $\boldsymbol{m}^{\mathsf{Z}}$. The differences in C_r caused by these approximations are minor; this is consistent with arguments and experiences discussed above. The predicted value of C_r falls in the range 0.09–0.10, but decreases slightly as Δ increases. As noted earlier, C_r tends to drop

TABLE IX
Elements of Resolved Enstrophy Dissipation

Δ/η	N	$\langle(\nabla\|\tilde{\mathbf{S}}\|)\cdot[\nabla\cdot(\tilde{\omega}\tilde{\omega})]\rangle$	$\langle\|\tilde{\mathbf{S}}\|\nabla\tilde{\omega} : \nabla\tilde{\omega}^{\mathsf{T}}\rangle$	$\langle\|\tilde{\mathbf{S}}\|\rangle\ \langle\nabla\tilde{\omega} : \nabla\tilde{\omega}^{\mathsf{T}}\rangle$
5	128	993.89	606217.	447272.
10	128	70.273	183983.	152996.
20	128	−11.983	25702.4	23734.9
40	128	−1.9094	1913.06	1863.79
80	128	−0.94686	105.093	105.173
6.5	64	98.505	101700.	85524.3
13	64	−43.951	23727.0	21853.8
26	64	−7.7209	2493.09	2413.51
52	64	0.15264	138.708	137.811

Note. Values are normalized by multiplying by ℓ/u'^3.

TABLE X

Model Constant C_r Obtained by the Dynamic Model

Δ/η	N	$\frac{\langle \boldsymbol{l}\cdot\boldsymbol{m}\rangle}{\langle \boldsymbol{m}\cdot\boldsymbol{m}\rangle}$	$\frac{\langle \boldsymbol{l}^{\mathrm{C}}\cdot\boldsymbol{m}\rangle}{\langle \boldsymbol{m}\cdot\boldsymbol{m}\rangle}$	$\frac{\langle \boldsymbol{l}\cdot\boldsymbol{m}^{\mathrm{D}}\rangle}{\langle \boldsymbol{m}^{\mathrm{D}}\cdot\boldsymbol{m}^{\mathrm{D}}\rangle}$	$\frac{\langle \boldsymbol{l}^{\mathrm{C}}\cdot\boldsymbol{m}^{\mathrm{D}}\rangle}{\langle \boldsymbol{m}^{\mathrm{D}}\cdot\boldsymbol{m}^{\mathrm{D}}\rangle}$
5	128	0.1042	0.1021	0.1040	0.1023
10	128	0.0980	0.0959	0.0978	0.0961
20	128	0.0948	0.0924	0.0946	0.0926
40	128	0.0920	0.0893	0.0923	0.0905
80	128	0.0699	0.0725	0.0789	0.0813
6.5	64	0.1035	0.1011	0.1031	0.1013
13	64	0.0944	0.0917	0.0943	0.0922
26	64	0.0839	0.0804	0.0838	0.0811
52	64	0.0887	0.0864	0.0951	0.0901

Note. Results are obtained for different filter sizes, using both the 64^3 and 128^3 DNS data sets.

appreciably as the filter size becomes very large. A similar drop at $\Delta \to \ell$ was recently observed for the Smagorinsky coefficient C_s [48], based on energy dissipation arguments. However, it was found that C_s also decreases in the limit of $\Delta \to \eta$ [48], while here no such decrease is observed for C_r. Since C_r depends on gradients of vorticity as opposed to velocity, it is plausible that C_r is less affected by viscosity than C_s at small scales.

Finally, Table XI compares the computed values of C_r using all three methods. The table shows that the predictions of the dynamic model are generally 18–25% higher than those obtained using methods 1 and 2. On the other hand, the predictions of the dynamic model are about 20% smaller than the theoretical value $C_r \approx 0.12$ obtained in Appendix A. Nonetheless, one may still note that the values of the model constant determined using the dynamic procedure are fairly consistent with those obtained from enstrophy balances.

TABLE XI

Model Constant C_r Obtained by: (a) Balancing Production and Dissipation of Resolved Enstrophy; (b) Balancing the Enstrophy Dissipation of the Real and Modeled SFS Torques; and (c) the Dynamic Procedure

Δ/η	N	C_r (a)	C_r (b)	C_r (c)
5	128	0.0858	0.0871	0.1042
10	128	0.0816	0.0827	0.0980
20	128	0.0772	0.0799	0.0948
40	128	0.0734	0.0822	0.0920
80	128	0.0591	0.0886	0.0699
6.5	64	0.0802	0.0843	0.1035
13	64	0.0767	0.0818	0.0944
26	64	0.0702	0.0799	0.0839
52	64	0.0601	0.0852	0.0887

5. A PRIORI TESTS OF PARTICLE APPROXIMATION

The objective of this section is to establish the ability of the particle representation (Section 3) to accurately determine the model coefficient and SFS torque. The analysis is based on comparing predictions of the particle approximation to the corresponding spectral values. The same DNS data is used to both determine the spectral values and to initialize the particle field. Specifically, the data are filtered by convolution with the third-order Gaussian core smoothing function (Eq. (43)). The convolution is performed on the DNS data in Fourier space. Based on the filtered DNS data spectral collocation estimates of $\tilde{\boldsymbol{u}}$, $\tilde{\mathbf{S}}$, and $\tilde{\omega}$ are then obtained in physical space. Also, $\boldsymbol{l}^{\mathsf{C}} = (\overline{\tilde{\boldsymbol{u}} \cdot \nabla \tilde{\omega}} - \bar{\tilde{\boldsymbol{u}}} \cdot \nabla \bar{\tilde{\omega}})$ and $\boldsymbol{m}^{\mathsf{D}}$ are computed, based on spectral differentiation and test-filtering at scale 2Δ with the cubic Gaussian. These are the "spectral" values at the collocation points.

To compute their particle approximation, we imagine placing particles at collocation points and associate the spectral values of $\tilde{\omega}$, $\tilde{\boldsymbol{u}}$, and $\tilde{\mathbf{S}}$ at those points with "particle values" there. Next, the terms $\boldsymbol{l}^{\mathsf{C}}$ and $\boldsymbol{m}^{\mathsf{D}}$ are computed from these particle values, according to the proposed scheme. Results are compared to the spectral values of $\boldsymbol{l}^{\mathsf{C}}$ and $\boldsymbol{m}^{\mathsf{D}}$. Some intermediate variables are also compared.

In the evaluation of Lagrangian derivatives (Eqs. (55) and (56)) the DNS data at two time levels, t and $t + \Delta t$, are used. The normalized time step is $\Delta t u'/\ell = 8.34 \times 10^{-3}$. In evaluating the particle vorticity at time $t + \Delta t$, the particle positions $\boldsymbol{X}_i(t)$ (initially the collocation points) are updated using a second-order predictor–corrector scheme to give $\boldsymbol{X}_i(t + \Delta t)$ (which typically no longer coincide with collocation points). The vorticities at $\boldsymbol{X}_i(t + \Delta t)$ are obtained by bilinear interpolation of the grid-based vorticity at time $t + \Delta t$. Equations (54)–(56) are then used to determine the Lagrangian derivatives $[\tilde{d}\tilde{\omega}/dt]$, $[\overline{\tilde{d}\tilde{\omega}}/dt]$, and $[\tilde{d}\bar{\tilde{\omega}}/dt]$, and consequently $\boldsymbol{l}^{\mathsf{C}}$. The diffusive terms in the expressions of $\boldsymbol{m}^{\mathsf{D}}$ require data at a single time level. The diffusion terms $\nabla \cdot (|\tilde{\mathbf{S}}| \nabla \tilde{\omega})$, $\overline{\nabla \cdot (|\tilde{\mathbf{S}}| \nabla \tilde{\omega})}$, and $\nabla \cdot (|\tilde{\mathbf{S}}| \nabla \bar{\tilde{\omega}})$ are found directly from the particle data following Eqs. (51)–(53). The results are then plugged into the definition of $\boldsymbol{m}^{\mathsf{D}}$ (Eq. (28)).

By adopting this simplified approach, the analysis addresses the validity of the particle approximation only. This represents a conservative approach, since the adopted initialization scheme is rather crude, and the particle distribution may be further tuned to provide better agreement with the DNS data. However, it is important to stress that this test does not address the performance of the actual Lagrangian vortex method, where the dynamical equations must be integrated over many time steps [14].

Tests are performed using four different particle distributions. In the first case, 64^3 particles are uniformly distributed in the domain; i.e., they are placed at the nodes of a uniform Cartesian grid. As mentioned above, we associate the particle strength with the local filtered vorticity; i.e., we set $\boldsymbol{\zeta}_i = \tilde{\omega}(\boldsymbol{X}_i)$. The volumes of the particles are $dV_i = h^3$, where h is the mesh size of the Cartesian grid. For the second case, the same number of particles is used, but the particles are randomly distributed within the domain; a uniform random distribution in 3D is used for this purpose. The third and fourth distributions are similar to the first and second, but they use a smaller number of particles, $N = 32^3$. Thus, the effect of particle density can be examined. Unless otherwise noted, tests are performed with a filter width $\Delta = 20\eta$.

At each particle position, all the quantities needed to determine $\boldsymbol{l}^{\mathsf{C}}$ and $\boldsymbol{m}^{\mathsf{D}}$ are computed using both the spectral and particle schemes. The spectral computations rely on the 128^3 DNS mesh. Since the filter size is significantly larger than the grid spacing, the filtered quantities are very smooth. Thus, the interpolation errors are found to be insignificant.

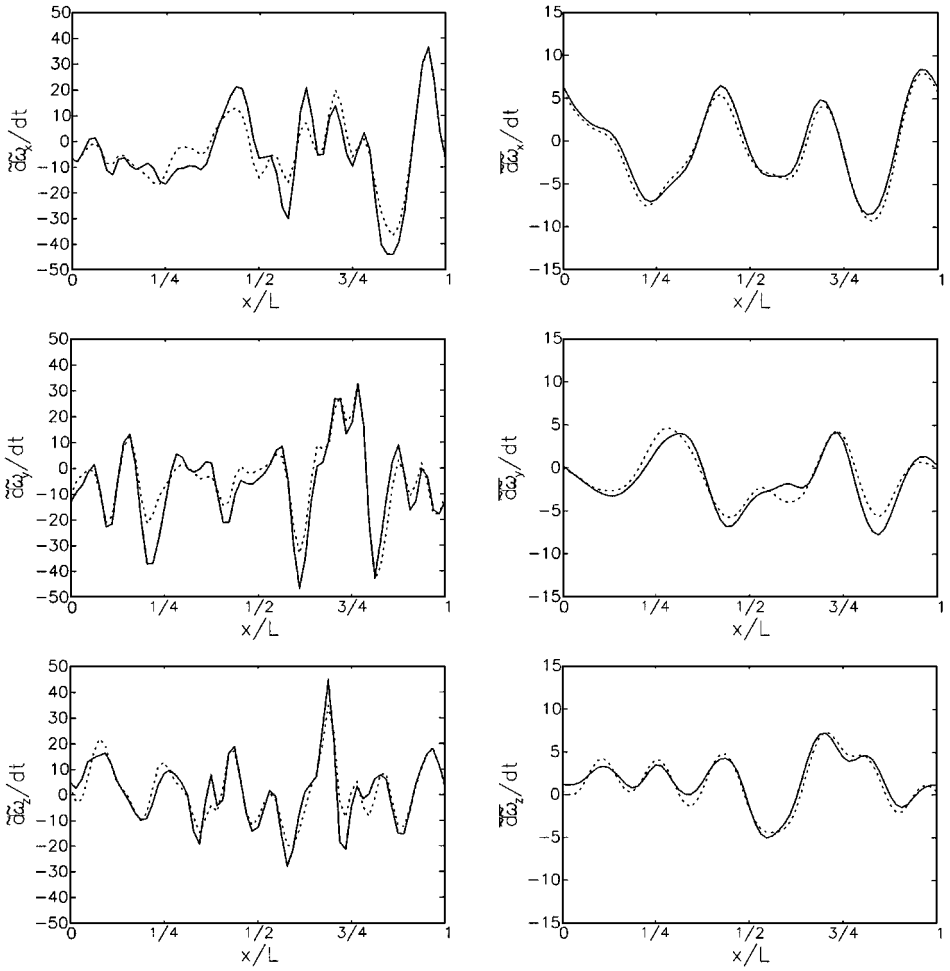

FIG. 10. Lagrangian derivatives of vorticity. Left: x, y, and z components of $\tilde{d}\tilde{\omega}/dt$, arranged from top. Right: x, y, and z components of $\overline{\tilde{d}\tilde{\omega}}/dt$, arranged from top. The Lagrangian calculations (dash) are obtained using a uniform distribution of 64^3 particles, while the spectral calculations (solid) are performed on a 128^3 grid. Values are normalized by $(u'/\ell)^2$.

5.1. *Regularly Placed Particles*

Comparison of spectral and particle predictions of various Lagrangian derivatives are provided in Figs. 10 and 11. The figures show 1D profiles along a selected line across the 3D domain. The results show that there is generally good agreement between the spectral and particle predictions of $\tilde{d}\tilde{\omega}/dt$. There is better agreement between the computed values of $\overline{\tilde{d}\tilde{\omega}}/dt$ and $\tilde{\bar{d}}\tilde{\bar{\omega}}/dt$, and it is hard to distinguish between the spectral and particle results for $\boldsymbol{I}^{\mathrm{C}}$.

Spectral and particle results for various filtered diffusion terms are shown in Figs. 12 and 13. The results for diffusion of grid filtered vorticity, $\nabla \cdot (|\tilde{\mathbf{S}}|\nabla\tilde{\omega})$, are in rough agreement. The particle method experiences its largest errors at the extreme values of the derivative. Note, however, that there is a better match between the predictions of the test-filtered diffusion terms. This leads to a good agreement between the results for $\boldsymbol{m}^{\mathrm{D}}$, although the extreme values appear to be slightly underestimated.

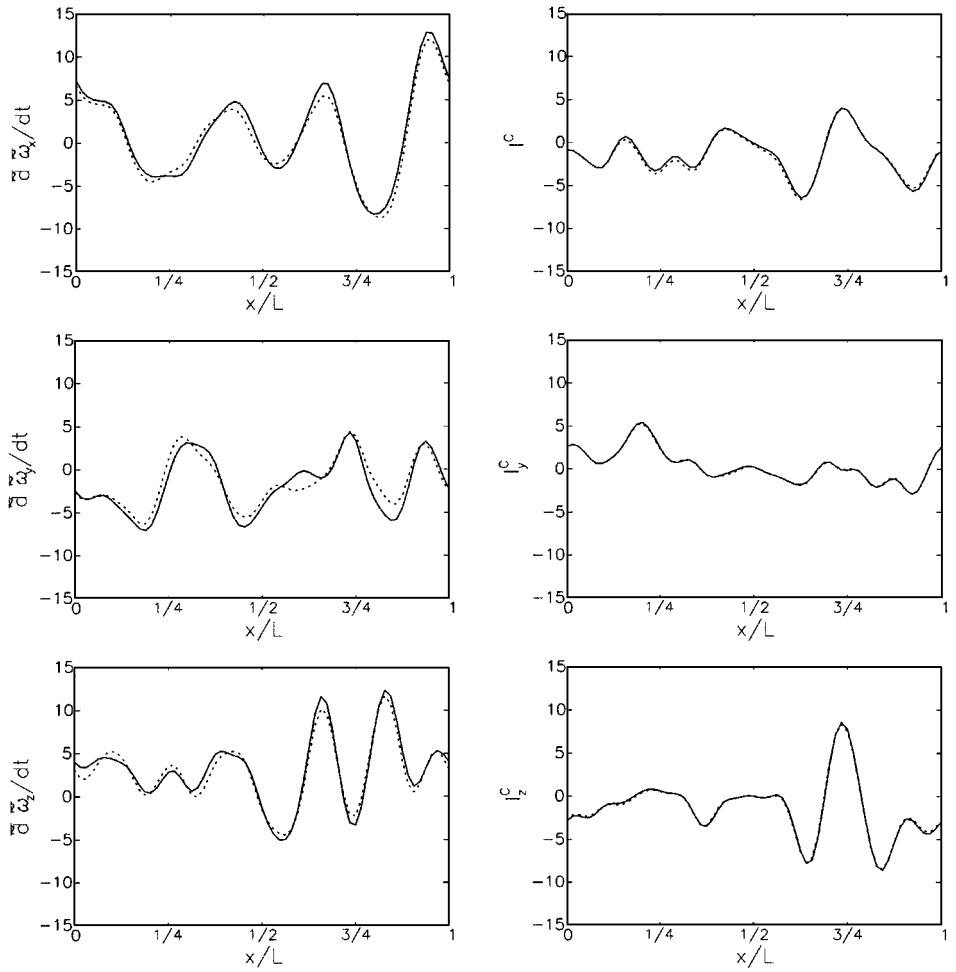

FIG. 11. Lagrangian derivatives of vorticity. Left: x, y, and z components of $\overline{\tilde{d}\tilde{\omega}}/dt$, arranged from top. Right: x, y, and z components of $\boldsymbol{I}^{\mathbf{C}}$, arranged from top. The Lagrangian calculations (dash) are obtained using a uniform distribution of 64^3 particles, while the spectral calculations (solid) are performed on a 128^3 grid. Values are normalized by $(u'/\ell)^2$.

In order to provide a global contrast of particle and spectral results we rely on scatter plots of 3D data sets. Such plots are provided in Figs. 14 and 15, which compare particle and spectral computations of Lagrangian vorticity derivatives and diffusion terms, respectively. The figures indicate that essential features in the 1D profiles are also, to a great extent, representative of the 3D data. In particular, the plots clearly illustrate that there is general agreement between particle and spectral computations and that the agreement is quite sharp for test-filtered quantities.

Another advantage of the scatter plots is that they enable us to extract quantitative global measures of the agreement between the Lagrangian and spectral predictions. Here, we simply rely on the slope of the least-squares linear fit of the data in the scatter plots, and on their linear correlation. Table XII gives the slopes of least-squares fits for selected vectors. For the same cases, results for the linear correlation are provided in Table XIII. Since the flow is isotropic, only the x-component of the vectors is considered in this analysis.

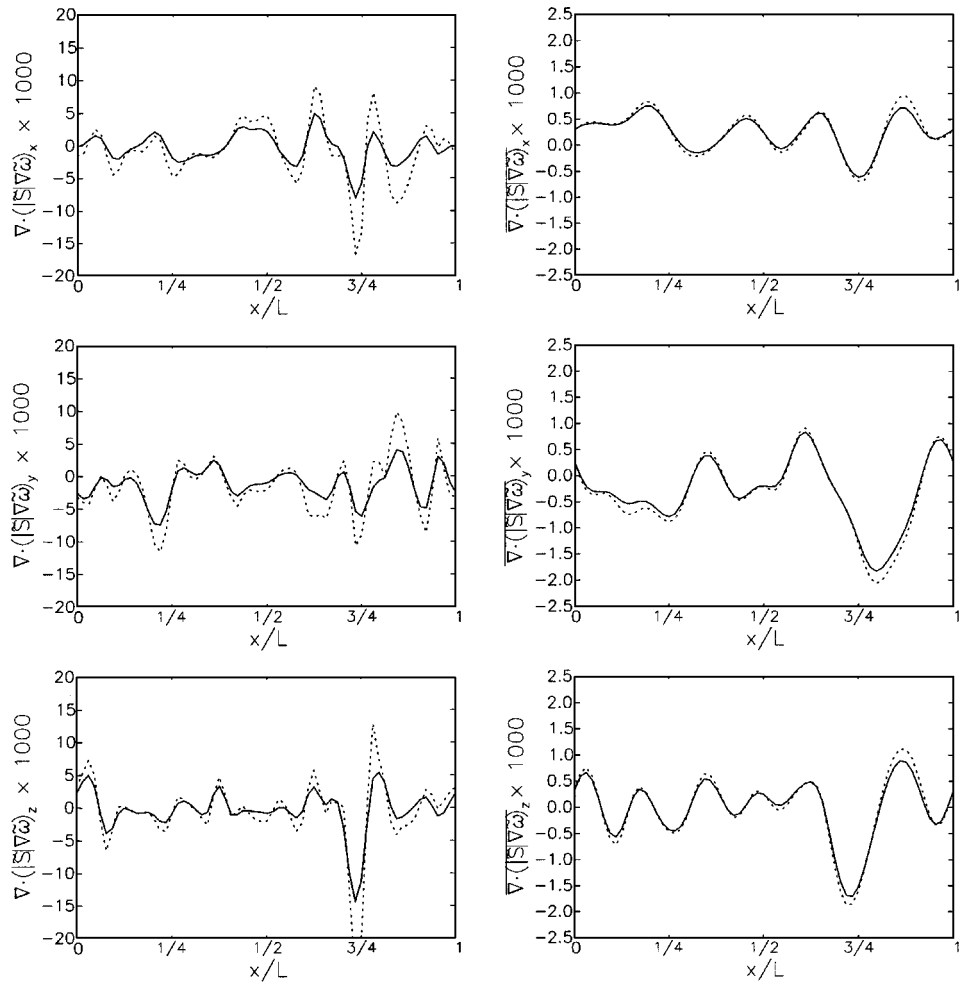

FIG. 12. Diffusion of resolved vorticity. Left: x, y, and z components of $\nabla \cdot (|\tilde{\mathbf{S}}|\nabla\tilde{\boldsymbol{\omega}})$, arranged from top. Right: x, y, and z components of $\nabla \cdot (|\tilde{\mathbf{S}}|\nabla\tilde{\boldsymbol{\omega}})$, arranged from top. The Lagrangian calculations (dash) are obtained using a uniform distribution of 64^3 particles, while the spectral calculations (solid) are performed on a 128^3 grid. Values are normalized by u'^2/ℓ^4.

Note that perfect agreement of the particle and spectral calculations would result in all points falling on a line through the origin with slope equal to one. This is nearly the case for I_x^{C}. It is interesting that the correlation of I_x^{C} is much better than that of either of the terms used to compute it, $\boldsymbol{I}^{\mathrm{C}} = \overline{\tilde{d}\tilde{\boldsymbol{\omega}}}/dt - \tilde{d}\bar{\tilde{\boldsymbol{\omega}}}/dt$. This suggests that errors in computing the Lagrangian derivatives are cancelled while taking the differences of filtered terms. The correlations of $\overline{\tilde{d}\tilde{\omega}_x}/dt$ and $\tilde{d}\bar{\tilde{\omega}}_x/dt$ are better than the correlation of $\tilde{d}\tilde{\omega}_x/dt$, which is still a respectable 0.914. The particle results for $\tilde{d}\tilde{\omega}_x/dt$ have a slope of 1.1, but the test-filtered predictions $\overline{\tilde{d}\tilde{\omega}_x}/dt$ and $\tilde{d}\bar{\tilde{\omega}}_x/dt$ have a slope of 0.98 and 1.04, respectively. Overall, a near unity slope of 1.008 for I_x^{C} is obtained.

Results of the Lagrangian calculations of diffusion terms are generally in good agreement with the corresponding spectral computations. Linear correlation coefficients fall in the range of 0.96–0.99 for all the diffusion terms. However, the slope of the linear fit for $\nabla \cdot (|\tilde{\mathbf{S}}|\nabla\tilde{\boldsymbol{\omega}})$ (0.632) is rather low. The high value of the linear correlation and the behavior

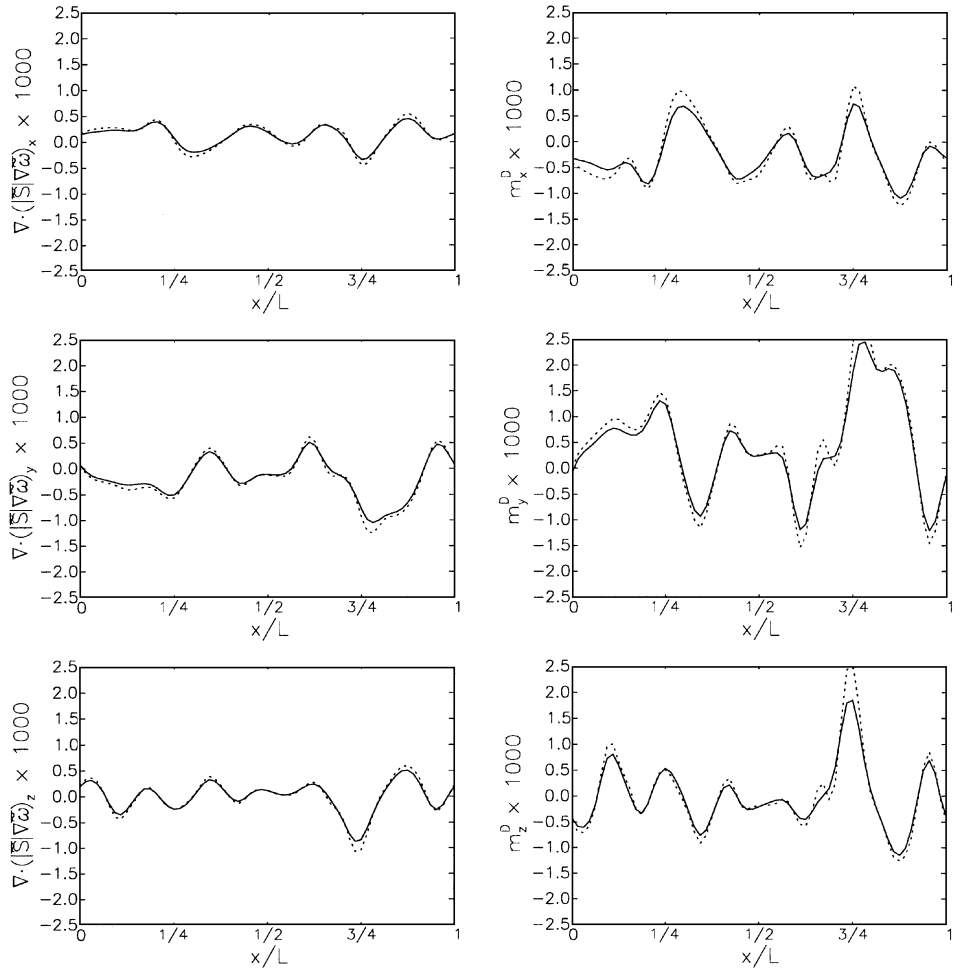

FIG. 13. Diffusion of resolved vorticity. Left: x, y, and z components of $\nabla \cdot (|\bar{\tilde{S}}|\nabla\bar{\omega})$, arranged from top. Right: x, y, and z components of $\boldsymbol{m}^D$, arranged from top. The Lagrangian calculations (dash) are obtained using a uniform distribution of 64^3 particles, while the spectral calculations (solid) are performed on a 128^3 grid. Values are normalized by u'^2/ℓ^4.

of the scatter plots indicate that the low value of the slope is due to underestimated predictions across the whole range of values and not just not just an attenuation of extreme events. With test filtering, the discrepancy drops to 12–17%. This suggests that the discrepancy is scale dependent and not due to a constant factor in the method.

5.2. *Variation of Parameters*

In Section 5.1, the numerical tests focused on a single Lagrangian discretization, with particle data initialized on a uniform grid. Here, we briefly examine the effects of a nonuniform distribution of particles, of particle density and filter width.

In order to examine the effect of an irregular distribution of particles the numerical tests are repeated using a random initial distribution, but with the same number of particles $N = 64^3$. Bilinear interpolation is used to obtain values at particle locations. One-dimensional profiles and scatter plots for the Lagrangian derivatives and for the diffusion terms have been

TABLE XII
Slope of Least-Squares Linear Fit of the Particle-Spectral Data

Filter width	$\Delta/\eta = 20$				$\Delta/\eta = 40$	
No. of particles	64^3		32^3		32^3	
Arrangement	Regular	Random	Regular	Random	Regular	Random
Quantity	Slope					
$\widetilde{d\tilde{\omega}_x/dt}$	1.103	1.006	1.103	1.007	1.042	1.001
$\overline{\widetilde{d\tilde{\omega}_x/dt}}$	0.983	1.000	0.983	1.015	0.996	1.005
$\widetilde{d\bar{\tilde{\omega}}_x/dt}$	1.046	1.001	1.001	1.013	1.018	1.011
I_x^C	1.008	0.993	1.006	0.969	1.005	0.999
$\nabla\cdot(\widetilde{\|\tilde{S}\|\nabla\tilde{\omega}_x})$	0.632	0.632	0.658	0.625	0.582	0.588
$\overline{\nabla\cdot(\widetilde{\|\tilde{S}\|\nabla\tilde{\omega}_x})}$	0.880	0.870	0.935	0.863	0.883	0.885
$\nabla\cdot(\widetilde{\|\tilde{S}\|\nabla\bar{\tilde{\omega}}_x})$	0.867	0.856	0.919	0.846	0.862	0.876
m_x^D	0.835	0.823	0.884	0.804	0.815	0.840

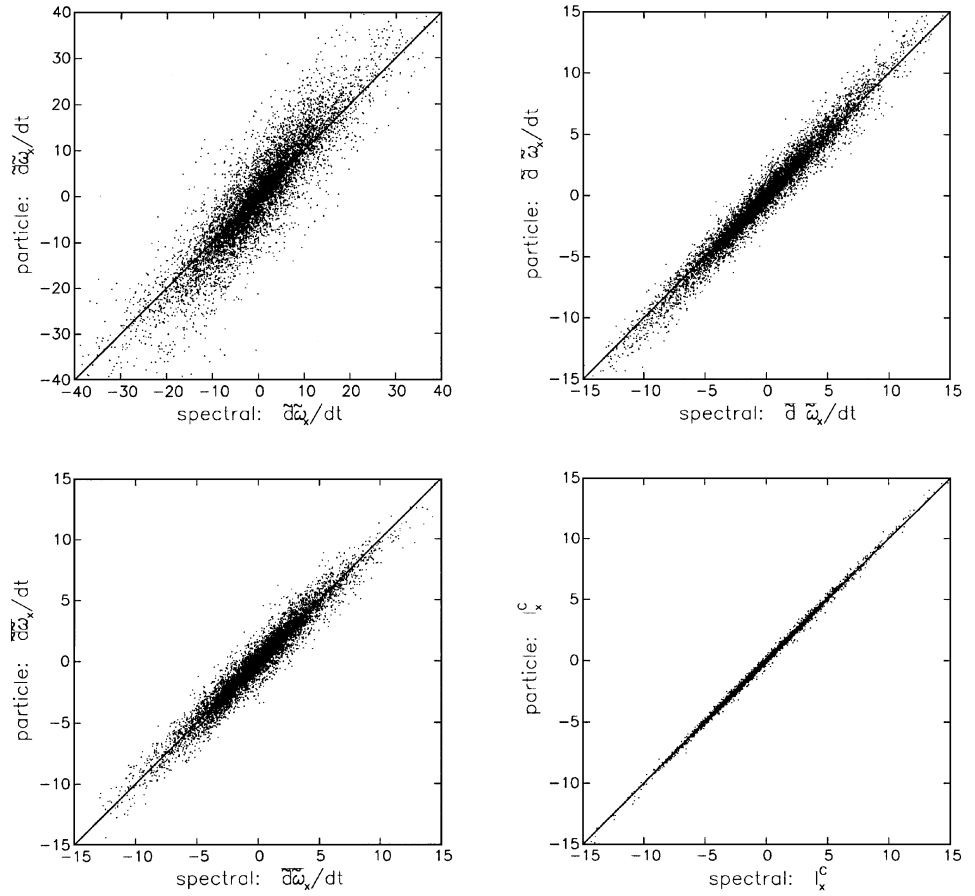

FIG. 14. Lagrangian derivatives of vorticity. The particle values, obtained using a regular distribution of 64^3 particles, are plotted against the corresponding spectral computations, performed on the 128^3 DNS grid.

TABLE XIII
Linear Correlation of Particle and Spectral Data

Filter width	$\Delta/\eta = 20$				$\Delta/\eta = 40$	
No. of particles	64^3		32^3		32^3	
Arrangement	Regular	Random	Regular	Random	Regular	Random
Quantity	Correlation					
$\tilde{d}\tilde{\omega}_x/dt$	0.914	0.972	0.914	0.972	0.984	0.995
$\overline{\tilde{d}\tilde{\omega}_x}/dt$	0.972	0.992	0.972	0.947	0.994	0.984
$\tilde{d}\bar{\tilde{\omega}}_x/dt$	0.984	0.989	0.984	0.932	0.997	0.986
l_x^C	0.999	0.988	0.999	0.922	1.000	0.986
$\nabla\cdot(\|\tilde{S}\|\nabla\tilde{\omega}_x)$	0.963	0.946	0.958	0.834	0.951	0.934
$\overline{\nabla\cdot(\|\tilde{S}\|\nabla\tilde{\omega}_x)}$	0.998	0.993	0.997	0.957	0.997	0.992
$\nabla\cdot(\|\tilde{S}\|\nabla\bar{\tilde{\omega}}_x)$	0.994	0.955	0.993	0.736	0.993	0.960
m_x^D	0.988	0.896	0.987	0.592	0.984	0.895

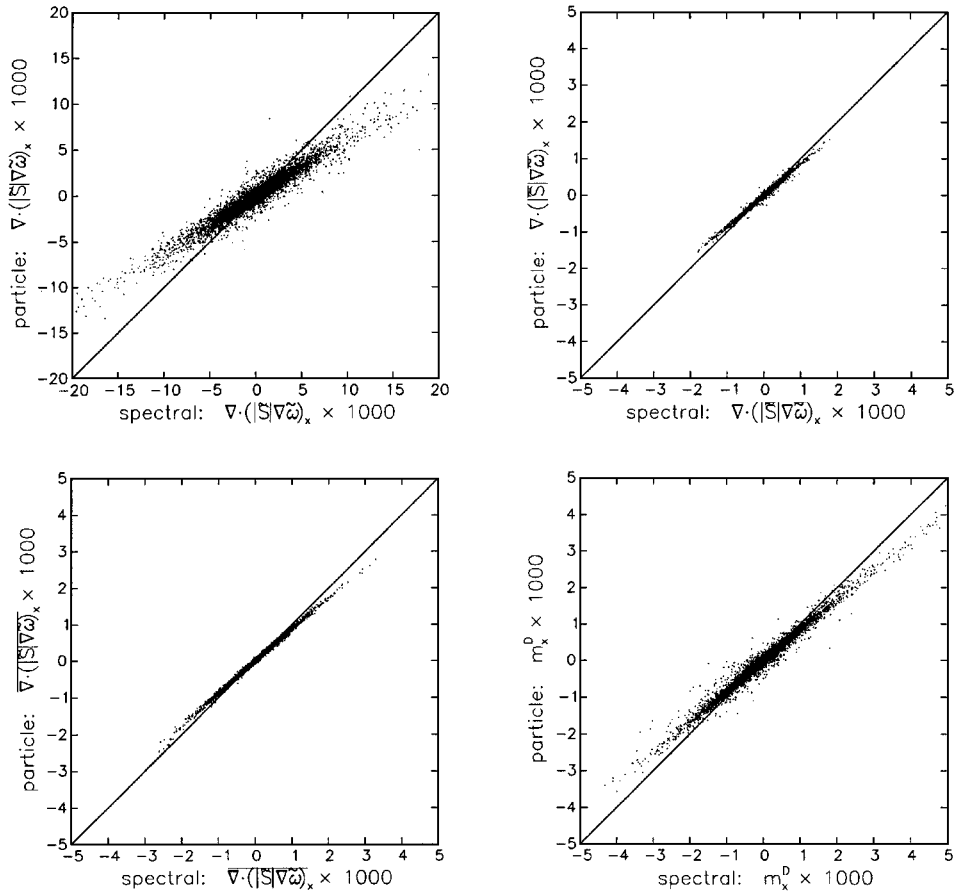

FIG. 15. Turbulent diffusion terms. The particle values, obtained using a regular distribution of 64^3 particles, are plotted against the corresponding spectral computations, performed on the 128^3 DNS grid.

obtained [49], but they are omitted since they exhibit essentially the same trends observed earlier. Thus, we focus exclusively on global measures. Our experience is that adopting a random distribution of particle positions slightly improves the correlation of the Lagrangian derivatives (Table XIII) and, more significantly, the slopes of the corresponding least-squares fits (Table XII). However, the correlation of l_x^{C} drops slightly, from 0.999 to 0.988. Thus, it appears that the systematic cancellation of errors that occurs while taking differences of Lagrangian derivatives (Section 5.1) depends on the spatial arrangement of particles. The random placement of particles has a slight negative impact on the diffusion terms. The correlations for $\nabla \cdot (|\tilde{\mathbf{S}}|\nabla\tilde{\omega}_x)$ and $\overline{\nabla \cdot (|\tilde{\mathbf{S}}|\nabla\tilde{\omega}_x)}$ appear unaffected by the change in particle arrangement. However, the correlations of $\nabla \cdot (|\tilde{\mathbf{S}}|\nabla\tilde{\omega}_x)$ and for $\boldsymbol{m}^{\mathsf{D}}$ both decrease, from 0.994 to 0.955 and from 0.988 to 0.896, respectively. Thus, the effect of the particle arrangement on the prediction of the diffusion terms is more noticeable. This is not surprising since the random arrangement may easily cause severe deterioration of an already crude particle strength initialization scheme.

The effects of particle density are analyzed in a similar fashion, and the results are also reported in Tables XII and XIII. Included are results obtained using 32^3 particles, both with regular and random particle distribution schemes. Briefly, when a regular arrangement is used the change in the number of particles has a very small impact on the predictions. On the other hand, when a random distribution of particles is used the reduction in number of particles leads to noticeable deterioration in the correlations with spectral results. Consistent with the discussion above, the effects are more pronounced for the diffusion terms.

Tables XII and XIII also provide results of tests conducted at larger filter width, $\Delta/\eta = 40$. The tests are repeated using 32^3 particles in order to keep the same filter width to particle spacing ratio. Briefly, the results are very similar to those obtained at smaller filter width and higher particle density and, consequently, lead to the same conclusions.

5.3. *Dynamic Model Coefficient*

Finally, the particle scheme is used to compute the dynamic model coefficient, C_r. As outlined in Section 3 (see also discussion in Section 4), C_r is obtained based on partial estimates of $\boldsymbol{l}$ and $\boldsymbol{m}$; specifically, we use

$$C_r \simeq \left(\frac{\langle \boldsymbol{l}^{\mathsf{C}} \cdot \boldsymbol{m}^{\mathsf{D}} \rangle}{\langle \boldsymbol{m}^{\mathsf{D}} \cdot \boldsymbol{m}^{\mathsf{D}} \rangle} \right)^{1/2}. \tag{73}$$

Results are given in Table XIV. For $N = 64^3$ and $\Delta/\eta = 20$, Table XIV shows that $C_r = 0.105$ when a regular distribution is used and $C_r = 0.095$ when a random distribution is employed. Both values are close to the spectral prediction, with differences of less than 10% and 0.5%, respectively. Good agreement is also obtained when a regular distribution with $N = 32^3$ is used. However, for a random distribution with $N = 32^3$, $C_r = 0.062$, roughly 35% lower than the spectral prediction. Dynamic predictions for $\Delta/\eta = 40$ and $N = 32^3$ match closely values calculated using $\Delta/\eta = 20$ and $N = 64^3$.

We conclude that for grid filter width $\Delta/\eta = 20$, 64^3 particles provide a sufficient resolution for adequate prediction of the model coefficient and the SFS torque. Good agreement with spectral predictions holds, whether the particles are arranged regularly or randomly. Results with 32^3 particles arranged regularly agree with results using the larger particle density, but the agreement is reduced at the lower particle density if the particles are arranged

TABLE XIV
Dynamic Model Coefficient Using the Particle Scheme

Δ/η	No. of particles	Arrangement	C_r
20	64^3	Regular	0.1052
20	64^3	Random	0.0952
20	32^3	Regular	0.1021
20	32^3	Random	0.0621
40	32^3	Regular	0.1070
40	32^3	Random	0.0950

randomly. Using a larger filter width and only 32^3 particles, however, maintains the resolution needed for the particle calculations to agree with the spectral calculations, regardless of particle placement.

6. SUMMARY AND CONCLUSIONS

A dynamic eddy diffusivity model is developed for large eddy simulation of the vorticity transport equation. The performance of the model is examined in light of *a priori* tests, based on results of direct numerical simulations of homogeneous, isotropic turbulence. Analysis of the real and modeled SFS torques leads to the following conclusions:

1. Subfilter scale vortex stretching and tilting is a significant contributor to the SFS overall torque. The contributions of SFS vortex stretching and tilting and of SFS convection of vorticity are poorly correlated and, consequently, may require different models.

2. The real subfilter scale torque is modeled using an eddy diffusivity term of the form $\nabla \times (\nu_T \nabla \times \tilde{\omega})$. The results indicate that this model shows fair correlation with the SFS torque due to vortex transport, but poor correlation with the SFS torque due to vortex stretching and tilting. Future extensions of the eddy diffusivity model (e.g., through similarity and mixed models) to improve on this weakness are desirable.

3. The SFS model can be expressed as the sum of a gradient diffusion term and a generalized transport term, due to variable eddy viscosity. Results show that the gradient diffusion part of the model is roughly one order of magnitude larger than the remaining part.

4. From a practical point of view, our main conclusion is that the coefficient of the eddy-viscosity model can be determined dynamically using filtering at two different scales in the context of a Lagrangian vortex model. The computed values of the dynamic model coefficient are consistent with those computed using resolved enstrophy balances.

Numerical experiments were also conducted to explore the implementation of the dynamic SFS model in a discretization that mimics a three-dimensional vortex method. The simplified model and dynamic procedure are then recast in a Lagrangian form which is based on a particle representation of the vorticity field. The values obtained from the particle discretization are compared to spectral values. The comparison shows that when sufficient resolution is provided the particle scheme yields reasonable predictions of both the SFS torques and the dynamic model constant.

Results of these *a priori* tests and previous experiences with vortex element computations are quite encouraging, despite the indicated weaknesses of the model. In [14] we take advantage of these results by applying the proposed dynamic LES scheme to a three-dimensional vortex element-based LES of high-Reynolds-number shear flow.

APPENDIX A: THEORETICAL DETERMINATION OF MODEL CONSTANT C_r FOR ISOTROPIC TURBULENCE

The traditional approach of determining the Smagorinsky coefficient C_s is based on a balance between energy production and SGS dissipation [15]. Analogously, determination of C_r may proceed, based on balancing enstrophy production and dissipation for homogeneous, isotropic turbulence. The scalar dot product of $\tilde{\boldsymbol{\omega}}$ with Eq. (11) results in the following equation of motion of the resolved enstrophy field:

$$\frac{\partial}{\partial t}\left(\frac{1}{2}\tilde{\omega}^2\right)+\tilde{\boldsymbol{u}}\cdot\nabla\left(\frac{1}{2}\tilde{\omega}^2\right)=\tilde{\boldsymbol{\omega}}\tilde{\boldsymbol{\omega}}:\tilde{\mathbf{S}}+\nu\nabla^2\left(\frac{1}{2}\tilde{\omega}^2\right)-\nu\nabla\tilde{\boldsymbol{\omega}}:\nabla\tilde{\boldsymbol{\omega}}^{\mathsf{T}}+\tilde{\boldsymbol{\omega}}\cdot\boldsymbol{r}+\tilde{\boldsymbol{\omega}}\cdot\nabla\times\boldsymbol{\mathcal{F}}. \tag{A.1}$$

Under the assumption of statistical homogeneity and stationarity, several terms average to zero, leaving a balance of resolved enstrophy generation by vortex stretching and large-scale forcing and dissipation by molecular viscosity and the subfilter scale torque:

$$0=[\langle\tilde{\boldsymbol{\omega}}\tilde{\boldsymbol{\omega}}:\tilde{\mathbf{S}}\rangle+\langle\tilde{\boldsymbol{\omega}}\cdot\nabla\times\boldsymbol{\mathcal{F}}\rangle]-[\langle\nu\nabla\tilde{\boldsymbol{\omega}}:\nabla\tilde{\boldsymbol{\omega}}^{\mathsf{T}}\rangle-\langle\tilde{\boldsymbol{\omega}}\cdot\boldsymbol{r}\rangle]. \tag{A.2}$$

Assuming that filtering is done in the inertial range and that forcing occurs at integral length scales only, scaling arguments show that

$$\langle\tilde{\boldsymbol{\omega}}\cdot\nabla\times\boldsymbol{\mathcal{F}}\rangle/\langle\tilde{\boldsymbol{\omega}}\tilde{\boldsymbol{\omega}}:\tilde{\mathrm{S}}\rangle\sim\Delta^2/\ell^2. \tag{A.3}$$

When $\Delta\ll\ell$, we have

$$\langle\tilde{\boldsymbol{\omega}}\cdot\nabla\times\boldsymbol{\mathcal{F}}\rangle\ll\langle\tilde{\boldsymbol{\omega}}\tilde{\boldsymbol{\omega}}:\tilde{\mathrm{S}}\rangle, \tag{A.4}$$

and the forcing term may be safely neglected in the resolved enstrophy balance.

After replacing the subfilter torque $\boldsymbol{r}$ with the model $\boldsymbol{g}$ (Eq. (15)), the resolved enstrophy equation becomes

$$0=\langle\tilde{\boldsymbol{\omega}}\tilde{\boldsymbol{\omega}}:\tilde{\mathbf{S}}\rangle-\langle(\nu+\nu_{\mathrm{T}})\nabla\tilde{\boldsymbol{\omega}}:\nabla\tilde{\boldsymbol{\omega}}^{\mathsf{T}}\rangle-\langle(\nabla\nu_{\mathrm{T}})\cdot[\nabla\cdot(\tilde{\boldsymbol{\omega}}\tilde{\boldsymbol{\omega}})]\rangle. \tag{A.5}$$

Substituting for ν_{T} from Eq. (16) we have

$$\begin{aligned}\langle\tilde{\omega}_i\tilde{\omega}_j\tilde{\mathrm{S}}_{ij}\rangle=\nu\left\langle\frac{\partial\tilde{\omega}_i}{\partial x_j}\frac{\partial\tilde{\omega}_i}{\partial x_j}\right\rangle+C_r^2\Delta^2\left\langle\sqrt{2\tilde{\mathrm{S}}_{mn}\tilde{\mathrm{S}}_{mn}}\frac{\partial\tilde{\omega}_i}{\partial x_j}\frac{\partial\tilde{\omega}_i}{\partial x_j}\right\rangle\\+C_r^2\Delta^2\left\langle\frac{\partial}{\partial x_j}\left(\sqrt{2\tilde{\mathrm{S}}_{mn}\tilde{\mathrm{S}}_{mn}}\right)\frac{\partial}{\partial x_i}(\tilde{\omega}_i\tilde{\omega}_j)\right\rangle,\end{aligned} \tag{A.6}$$

from which C_r may be determined.

At large enough filter scale ($\Delta\gg\eta$, where η is the Kolmogorov scale), viscous dissipation is negligible compared to subgrid scale dissipation. Also, as discussed in Section 4,

$$\langle(\nabla\|\tilde{\mathbf{S}}\|)\cdot[\nabla\cdot(\tilde{\boldsymbol{\omega}}\tilde{\boldsymbol{\omega}})]\rangle\ll\langle\|\tilde{\mathbf{S}}\|\nabla\tilde{\boldsymbol{\omega}}:\nabla\tilde{\boldsymbol{\omega}}^{\mathsf{T}}\rangle, \tag{A.7}$$

so that

$$\langle \tilde{\omega}_i \tilde{\omega}_j \tilde{\mathsf{S}}_{ij} \rangle \approx (C_r \Delta)^2 \left\langle \sqrt{2\tilde{\mathsf{S}}_{mn}\tilde{\mathsf{S}}_{mn}} \frac{\partial \tilde{\omega}_i}{\partial x_j} \frac{\partial \tilde{\omega}_i}{\partial x_j} \right\rangle. \tag{A.8}$$

Next, assuming that the strain rate norm and the vorticity gradient norm are uncorrelated and that

$$\left\langle \sqrt{\tilde{\mathsf{S}}_{mn}\tilde{\mathsf{S}}_{mn}} \right\rangle \approx \langle \tilde{\mathsf{S}}_{mn}\tilde{\mathsf{S}}_{mn} \rangle^{1/2}, \tag{A.9}$$

we obtain

$$\left\langle \sqrt{2\tilde{\mathsf{S}}_{mn}\tilde{\mathsf{S}}_{mn}} \frac{\partial \tilde{\omega}_i}{\partial x_j} \frac{\partial \tilde{\omega}_i}{\partial x_j} \right\rangle \approx \sqrt{2} \langle \tilde{\mathsf{S}}_{mn}\tilde{\mathsf{S}}_{mn} \rangle^{1/2} \left\langle \frac{\partial \tilde{\omega}_i}{\partial x_j} \frac{\partial \tilde{\omega}_i}{\partial x_j} \right\rangle. \tag{A.10}$$

Similar assumptions of lack of correlation and of commutability of averaging with taking the square root were made by Lilly [15] and Scotti *et al.* [50]. Results in Section 4 show that these assumptions are in fact reasonable.

Kinematic relations for isotropic, incompressible turbulence give

$$\langle \tilde{\omega}_i \tilde{\omega}_j \tilde{\mathsf{S}}_{ij} \rangle = -\frac{35}{2} \left\langle \left(\frac{\partial \tilde{u}_1}{\partial x_1} \right)^3 \right\rangle, \tag{A.11}$$

$$\langle \tilde{\mathsf{S}}_{ij} \tilde{\mathsf{S}}_{ij} \rangle = \frac{15}{2} \left\langle \left(\frac{\partial \tilde{u}_1}{\partial x_1} \right)^2 \right\rangle. \tag{A.12}$$

Substituting Eq. (A.12) into Eq. (A.10), and Eqs. (A.10) and (A.11) into (A.8) results in

$$-\frac{35}{2} \left\langle \left(\frac{\partial \tilde{u}_1}{\partial x_1} \right)^3 \right\rangle \approx C_r^2 \Delta^2 \sqrt{15} \left\langle \left(\frac{\partial \tilde{u}_1}{\partial x_1} \right)^2 \right\rangle^{1/2} \left\langle \frac{\partial \tilde{\omega}_i}{\partial x_j} \frac{\partial \tilde{\omega}_i}{\partial x_j} \right\rangle. \tag{A.13}$$

It follows that

$$C_r^2 \approx \frac{35}{15^{3/2}} |S_3| \frac{\langle \tilde{\mathsf{S}}_{ij} \tilde{\mathsf{S}}_{ij} \rangle}{\Delta^2 \left\langle \frac{\partial \tilde{\omega}_m}{\partial x_n} \frac{\partial \tilde{\omega}_m}{\partial x_n} \right\rangle}, \tag{A.14}$$

where

$$S_3 = \left\langle \left(\frac{\partial \tilde{u}_1}{\partial x_1} \right)^3 \right\rangle \Bigg/ \left\langle \left(\frac{\partial \tilde{u}_1}{\partial x_1} \right)^2 \right\rangle^{3/2} \tag{A.15}$$

is the skewness of the filtered velocity derivative. The energy spectra of homogeneous, isotropic turbulence provides the ratio of the norms of the filtered strain rate and filtered vorticity gradient,

$$\frac{\langle \tilde{\mathsf{S}}_{ij} \tilde{\mathsf{S}}_{ij} \rangle}{\Delta^2 \left\langle \frac{\partial \tilde{\omega}_m}{\partial x_n} \frac{\partial \tilde{\omega}_m}{\partial x_n} \right\rangle} = \frac{2 \int_0^\infty |\hat{G}_\Delta(k)|^2 k^2 E(k)\, dk}{\Delta^2 2 \int_0^\infty |\hat{G}_\Delta(k)|^2 k^4 E(k)\, dk}, \tag{A.16}$$

where $E(k)$ is the turbulence 3D energy spectrum and $|\hat{G}_\Delta(k)|^2$ is the filter spectrum. Since it is assumed that the filter cuts off somewhere within the inertial range, the Kolmogorov spectrum $E(k) = C_k \epsilon^{2/3} k^{-5/3}$ may be used. The filter $G_\Delta(k)$ is taken to be the Fourier transform of the third-order Gaussian core-smoothing function. Numerical integration gives

$$\langle \tilde{\mathsf{S}}_{ij} \tilde{\mathsf{S}}_{ij} \rangle / \Delta^2 \left\langle \frac{\partial \tilde{\omega}_m}{\partial x_n} \frac{\partial \tilde{\omega}_m}{\partial x_n} \right\rangle \doteq 0.06098. \tag{A.17}$$

The skewness S_3 can be measured by filtering experimental or DNS velocity signals. While a dependence on filter size is typically observed [45], a representative value is $S_3 \approx -0.4$. Using $|S_3| = 0.4$ leads to $C_r = 0.12$, as mentioned in Section 2.

ACKNOWLEDGMENTS

We thank Mr. S. Cerutti for his help with the DNS data base of isotropic turbulence. This work was supported in part by the National Science Foundation through Grant ECS-9424432 and Grant CTS-9408344 and by the Office of Naval Research through Grant N00014-97-10429. Computer resources were provided through NSF Equipment Grant CTS-9506077 and by the Pittsburgh Supercomputer Center under NSF Grant CTS-930041P.

REFERENCES

1. A. Leonard, Energy cascade in large-eddy simulations of turbulent fluid flows, *Adv. Geophys.* **18**, 237 (1974).
2. R. Rogallo and P. Moin, Numerical simulation of turbulent flows, *Ann. Rev. Fluid Mech.* **16**, 99 (1984).
3. M. Lesieur and O. Metais, New trends in large-eddy simulations of turbulence, *Annu. Rev. Fluid Mech.* **28**, 45 (1996).
4. W. E and J.-G. Liu, Finite difference methods for 3D viscous incompressible flows in the vorticity-vector potential formulation on non-staggered grids, *J. Comput. Phys.* **138**, 57 (1997).
5. O. Daube, Resolution of the 2D Navier–Stokes equations in velocity–vorticity form by means of an influence matrix technique, *J. Comput. Phys.* **103**, 402 (1992).
6. O. M. Knio, A. S. Worlikar, and H. N. Najm, Mixing and chemical reaction in an idealized swirl chamber, in *Twenty-Sixth Symposium (International) on Combustion, 1996*, p. 203.
7. A. J. Chorin, Hairpin removal in vortex interactions, II, *J. Comput. Phys.* **107**, 1 (1993).
8. A. J. Chorin, *Vorticity and Turbulence* (Springer-Verlag, New York/Berlin, 1993).
9. A. J. Chorin, Microstructure, renormalization, and more efficient vortex methods, *ESAIM Proc.* **1**, 1 (1996).
10. P. S. Bernard, A vortex method for wall bounded turbulent flows, *ESAIM Proc.* **1**, 15 (1996).
11. J.-C. Saghbini, *Simulation of Vorticity Dynamics in Swirling Flows, Mixing and Vortex Breakdown*, M.Sc. thesis, Department of Mechanical Engineering, Massachusetts Institute of Technology, 1996.
12. V. M. Fernandez, N. J. Zabusky, P. Liu, S. Bhatt, and A. Gerasoulis, Filament surgery and temporal grid adaptivity extensions to a parallel tree code for simulation and diagnosis in 3D vortex dynamics, *ESAIM Proc.* **1**, 197 (1996).
13. G. S. Winckelmans, T. S. Lund, D. Carati, and A. A. Wray, A priori testing of subgrid-scale models for the velocity–pressure and velocity–vorticity formulations, in *Center of Turbulence Research Proceedings of the Summer Program, 1996*, p. 309.
14. J. R. Mansfield, O. M. Knio, and C. Meneveau, Dynamic LES of colliding vortex rings using a 3D vortex method, *J. Comput. Phys.*, submitted.
15. D. K. Lilly, The representation of small-scale turbulence in numerical simulation experiments, in *Proc. IBM Scientific Computing Symposium on Environmental Sciences, 1967*, p. 195.
16. J. Smagorinsky, General circulation experiments with the primitive equations. I. The basic experiment, *Mon. Weather Rev.* **91**, 99 (1963).

17. M. Germano, U. Piomelli, P. Moin, and W. H. Cabot, A dynamic subgrid-scale eddy viscosity model, *Phys. Fluids A* **3**, 1760 (1991).
18. P. Moin, K. Squires, W. Cabot, and S. Lee, A dynamic subgrid-scale model for compressible turbulence and scalar transport, *Phys. Fluids A* **3**, 2746 (1991).
19. U. Piomelli, High Reynolds number calculations using the dynamic subgrid-scale stress model, *Phys. Fluids A* **5**, 1484 (1993).
20. K. Akselvoll and P. Moin, Application of the dynamic localization model to large-eddy simulation of turbulent flow over a backward facing step, in *Engineering Applications of Large Eddy Simulations*, edited by U. Piomelli and S. Ragab (ASME., New York, 1993), FED 162:1.
21. J. Bardina, J. H. Ferziger, and W. C. Reynolds, Improved Subgrid Scale Models for Large Eddy Simulation, AIAA Paper 80-1357 (1980).
22. S. Liu, C. Meneveau, and J. Katz, On the properties of similarity subgrid-scale models as deduced from measurements in a turbulent jet, *J. Fluid Mech.* **275**, 83 (1994).
23. V. Borue and S. Orszag, Numerical study of three-dimensional Kolmogorov flow at high Reynolds numbers, *J. Fluid Mech.* **306**, 293 (1995).
24. U. Piomelli, Y. Yu, and R. Adrian, Subgrid-scale energy transfer and near-wall turbulence structure, *Phys. Fluids* **8**, 215 (1996).
25. J. O'Neil and C. Meneveau, Subgrid-scale stresses and their modeling in the turbulent plane wake, *J. Fluid Mech.* **349**, 253 (1997).
26. S. Liu, J. Katz, and C. Meneveau, Evolution and modeling of subgrid scales during rapid straining of turbulence, *J. Fluid Mech.*, submitted.
27. Y. Zang, R. L. Street, and J. Koseff, A dynamic mixed subgrid-scale model and its application to turbulent recirculating flows, *Phys. Fluids A* **5**, 3186 (1993).
28. X. Wu and K. Squires, Large eddy simulation of a canonical three-dimensional boundary layer, in *Proc. Tenth Symp. on Turbulent Shear Flows, Penn State, 1995*, edited by F. Durst, B. E. Launder, F. W. Schmidt, and J. W. Whitelaw.
29. K. Horiuti, A new dynamic two-parameter mixed model for large-eddy simulation, *Phys. Fluids* **9**, 3443 (1997).
30. B. Vreman, B. Geurts, and H. Kuerten, Large eddy simulation of the turbulent mixing layer, *J. Fluid Mech.* **339**, 357 (1997).
31. J. R. Mansfield, O. M. Knio, and C. Meneveau, Towards large vortex simulation, *ESAIM Proc.* **1**, 49 (1996).
32. D. K. Lilly, A proposed modification of the Germano subgrid scale closure method, *Phys. Fluids A* **4**, 633 (1992).
33. S. Ghosal, T. S. Lund, P. Moin, and K. Akselvoll, A dynamic localization model for large eddy simulation of turbulent flow, *J. Fluid Mech.* **286**, 229 (1995).
34. C. Meneveau, T. Lund, and W. Cabot, A Lagrangian dynamic subgrid-scale model of turbulence, *J. Fluid Mech.* **319**, 353 (1996).
35. A. Leonard, Computing three-dimensional incompressible flows with vortex elements, *Ann. Rev. Fluid Mech.* **17**, 525 (1985).
36. A. Chorin, *Vortex Methods*, Les Houches Summer School of Theoretical Physics, 1993.
37. E. Meiburg, Three-dimensional vortex dynamics simulations, in *Fluid Vortices*, edited by S. I. Green (Springer-Verlag, New York, 1995), p. 651.
38. G. K. Batchelor, *An Introduction to Fluid Dynamics* (Cambridge Univ. Press, Cambridge, 1967).
39. O. H. Hald, Convergence of vortex methods for Euler's equations, II, *SIAM J. Numer. Anal.* **16**, 726 (1979).
40. J. T. Beale and A. Majda, High-order accurate vortex method with explicit velocity kernels, *J. Comput. Phys.* **58**, 188 (1985).
41. J. T. Beale, A convergent 3D vortex method with grid-free stretching, *Math. Comput.* **46**, 401 (1986).
42. A. Leonard, Vortex methods for flow simulation, *J. Comput. Phys.* **37**, 289 (1980).
43. P. Degond and S. Mas-Gallic, The weighted particle method for convection-diffusion equations. Part I. The case of an isotropic viscosity; Part II. The anisotropic case, *Math. Comput.* **53**, 485 (1989).

44. O. M. Knio and A. F. Ghoniem, Three-dimensional vortex simulation of rollup and entrainment in a shear layer, *J. Comput. Phys.* **97**, 172 (1991).
45. S. Cerutti, C. Meneveau, and O. M. Knio, Statistical equilibrium in isotropic turbulence: Implications for hyperviscous and nonlocal subgrid models, in preparation.
46. C. Canuto, M. Y. Hussaini, A. Quarteroni, and T. A. Zang, *Spectral Methods in Fluid Dynamics* (Springer-Verlag, New York/Berlin, 1988).
47. A. Vincent and A. Meneguzzi, The spatial structure and statistical properties of homogeneous turbulence, *J. Fluid Mech.* **225**, 1 (1991).
48. C. Meneveau and T. S. Lund, The dynamic Smagorinsky model and scale-dependent coefficients in the viscous range of turbulence, *Phys. Fluids* **9**, 3932 (1997).
49. J. R. Mansfield, *A Dynamic Lagrangian LES Scheme for the Vorticity Transport Equation*, Ph.D. thesis, Johns Hopkins University, 1997.
50. A. Scotti, C. Meneveau, and D. K. Lilly, Generalized Smagorinsky model for anisotropic grids, *Phys. Fluids A* **5**, 2306 (1993).